



HAL
open science

Real-time distributed monitoring of pressure and shock velocity by ultrafast spectrometry with Chirped Fiber Bragg Gratings: Experimental vs calculated wavelength-to-pressure sensitivities in the range [0–4 GPa]

Sylvain Magne, Y. Barbarin, A. Lefrançois, M. Balbarie, F. Sinatti, A. Osmont, J. Luc, K. Woirin

► To cite this version:

Sylvain Magne, Y. Barbarin, A. Lefrançois, M. Balbarie, F. Sinatti, et al.. Real-time distributed monitoring of pressure and shock velocity by ultrafast spectrometry with Chirped Fiber Bragg Gratings: Experimental vs calculated wavelength-to-pressure sensitivities in the range [0–4 GPa]. *Journal of Applied Physics*, 2018, 124 (14), pp.145902. 10.1063/1.5031832 . hal-04559057

HAL Id: hal-04559057

<https://hal.science/hal-04559057>

Submitted on 25 Apr 2024

HAL is a multi-disciplinary open access archive for the deposit and dissemination of scientific research documents, whether they are published or not. The documents may come from teaching and research institutions in France or abroad, or from public or private research centers.

L'archive ouverte pluridisciplinaire **HAL**, est destinée au dépôt et à la diffusion de documents scientifiques de niveau recherche, publiés ou non, émanant des établissements d'enseignement et de recherche français ou étrangers, des laboratoires publics ou privés.



Distributed under a Creative Commons Attribution 4.0 International License

Real-time Distributed Monitoring of Pressure and Shock Velocity by ultrafast spectrometry with Chirped Fiber Bragg Gratings: Experimental vs Calculated Wavelength-to-Pressure Sensitivities in the Range [0 – 4 GPa]

S. Magne,^{1,a)} Y. Barbarin,²⁾ A. Lefrançois,²⁾ M. Balbarie,²⁾ F. Sinatti,²⁾ A. Osmont,²⁾ J. Luc,²⁾ K. Woirin³⁾

¹CEA, LIST, Laboratoire Capteurs Architectures Electroniques, F-91191 Gif-sur-Yvette cedex, France

²CEA, DAM, CEA-GRAMAT, F-46500 Gramat, France

³ArianeGroup, CRB, F-91710 Vert-le-Petit, France

Fiber Bragg Gratings (FBGs) are gaining acceptance as velocity/pressure gauges in the fields of detonation and shock physics on account of their sensitivity, small size, flexibility, electromagnetic immunity and wavelength-encoded capability. Chirped FBGs (CFBGs) are investigated as wavelength-to-position discriminators with the purpose of monitoring pressure/velocity profiles over a distance range of typically 100 mm. The use of CFBGs simplifies both sensor deployment and data retrieval and finally improves the accuracy due to the increased number of data points. In this paper, the metrological performance of CFBGs used as *in situ* distributed shock pressure/velocity gauges is investigated both theoretically and experimentally in planar shock loading configuration with Aluminum-based flyer and target. In the intermediate range for shock stress, *i.e.* less than the HEL of Silica, CFBGs provide simultaneous measurements of both shockwave velocity and stress within the target material. A Bragg wavelength-to-stress model is proposed that takes into account (i) the state-of-stress within the target material, (ii) the stress coupling coefficient due to imperfect impedance matching between the target material and the Silica fiber, (iii) the conversion of the state-of-stress into a state-of-strain within the Silica fiber and (iv) the conversion of strain data into observable Bragg wavelength shifts. Finally, the model also takes into account the pressure dependence of constitutive parameters for Silica and usual metals. An experimental calibration of CFBG as stress gauge under planar shock loading is performed with CFBGs bonded along the target axis with glue. 6061-T6 Aluminum flyers were launched at several velocities by a gas gun over transfer plates of similar material. A free-space Czerny-Turner and an integrated-optics AWG spectrometers were both used as spectrum analyzers. Experimental Bragg wavelength shifts agree well with theoretical predictions for both elastic and hydrodynamic domains of 6061-T6 Aluminum, opening up large perspectives for shock physics.

Author to whom correspondence should be addressed. sylvain.magne@cea.fr.

I. INTRODUCTION

The accurate measurement of shock and detonation parameters of High Explosives (HEs), such as the shock velocity U , the detonation velocity V_D , and the pressure P is essential to improve their design and manufacturing conditions as well as qualifying safety, damage and aging. Indeed, in the insensitive munitions process development, compression, shock performance and vulnerability experiments are performed, especially to identify the mechanical behavior of HEs, their Equations Of State (EOS) and reaction properties. Depending on formulations, the pressure conditions range from 0.5 GPa and 40 GPa and U ranges from 2 to 9 km/s. *In-situ* shock velocity measurements are provided by Electrical-Shorting Pins (ESP, uncertainty $\sim \pm 1.2\%$), drilled fibers ($\sim \pm 2.1\%$) or Photonic-Doppler Velocimetry (PDV, $\sim \pm 0.3\%$ with liquid TMETN).¹ *In-situ* pressure measurements are provided by Carbon or Manganin piezoresistive gauges (uncertainty $\sim \pm 7\%$).²⁻³ Finally, particle velocities are mostly determined by VISAR⁴ (Velocity Interferometer System for Any Reflector) over PMMA/LiF rear windows ($\sim \pm 0.1\%$) or magnetic gauges embedded within the material.⁵

The improvement of current dynamic instrumentation is still challenging in terms of response time, accuracy and spatial resolution. Moreover, the accurate monitoring of transient phenomena (*e.g.* Shock-to-Detonation-Transition - SDT –, Deflagration-to-Detonation-Transition – DDT-) involves the accurate measurement of the time delay between shock and reaction, for instance, with the help of wedge setups involving multiple gauges assembled in parallel at different distances to preserve 1-D shockwave front. The greater the number of gauges, the better the resolution in time. The installation of a wedge test is somehow complex and time-consuming both in sensor deployment and data analysis. Therefore, distributed measurements (*i.e.* multiple data over a single acquisition channel) are desirable in order to simplify the instrumentation and improve the accuracy of time delay measurements.

Fiber Bragg Gratings (FBGs) have been investigated during the last ten years as *in situ* pressure and velocity gauges in shock-loading experiments. A significant experimental feedback has been gained on velocity measurements.⁶⁻¹⁰ *In situ* pressure monitoring experiments involving FBGs were performed as well with short-length FBGs¹¹⁻¹⁶ or Chirped FBGs (CFBGs).¹⁷⁻¹⁸ However, an accurate relation linking the Bragg wavelength shift to the shock stress (*i.e.* wavelength-to-stress) is required. As the constitutive equation of the FBG involves the state-of-strain, two models are necessary: (i) a stress-to-strain model, (ii) a wavelength-to-strain model. Several ones have been proposed according to experimental shock conditions, mainly hydrostatic or planar. Unfortunately, these models are not accurate enough as large differences are still observed between experimental and predicted Bragg shifts.

In this paper, we investigate the wavelength-to-stress sensitivity of CFBGs used as *in situ* pressure gauges in inert planar shock loading conditions. The first part of the paper provides a theoretical analysis of the Bragg wavelength-to-stress sensitivity in the intermediate stress range [0 – 4 GPa], below the Hugoniot Elastic Limit (HEL) of Silica. The second part of the paper describes an experimental calibration in planar shock loading condition, achieved by the impact of Aluminum flyers launched at several velocities by a gas gun over transfer plates of similar material.

II. FIBER BRAGG GRATING (FBG) AS PRESSURE/VELOCITY SENSOR FOR SHOCK EXPERIMENTS

Fiber Bragg Gratings (FBGs) are widely used as strain/pressure sensors in many applications (civil engineering, structural health monitoring, oil & gas, etc.). They are obtained by photowriting a focused periodical fringe pattern into the UV-photosensitive fiber core using laser interferometry processes. A FBG is an ultra-low loss spectral filter that reflects light backwards. For a several millimeter-long FBG, the bandwidth (Full-Width at Half-Maximum – FWHM) is about 0.2 nm to 0.5 nm, the reflectivity might be adjusted between 0% and 100% (saturated FBG), and the Bragg wavelength λ_B is given by the well-known Bragg relation¹⁹⁻²⁰:

$$\lambda_B = 2 \cdot n \cdot \Lambda \quad (1)$$

where n is the effective index for the propagating mode and Λ is the pitch period of the fringe pattern.

In the following, the effective index will be considered identical to the bulk refractive index (RI) on account of the small index difference between fiber core and cladding.

FBGs are standardized by the telecommunication-based ITU grid (*International Telecommunication Union*). Multiplexing (Wavelength-Division Multiplexing – WDM) is enabled by wavelength-encoded signal capability. The spectral signature of the Bragg signal provides reliable measurements even in harsh conditions. Their use in shock physics is motivated by the high-bandwidth, passive nature, electromagnetic immunity, flexibility and small diameter (~ 150 μm with a Polyimide coating) of Silica-based optical fibers, minimizing perturbations due to impedance mismatch. While usual FBGs are considered as point sensors (several-mm long), chirped FBGs (CFBG) are used to provide wavelength-to-position discrimination with the purpose of monitoring pressure and velocity profiles over extended ranges of typically 100 mm. In planar shock loading experiments, the Hugoniot Elastic Limit (HEL) of Silica fibers is ~ 8.8 GPa.²¹⁻²² For impact stress in excess of the HEL, Silica undergoes a phase transition (with permanent densification) and is destroyed for stress levels above 16 GPa. Finally, a last - but not least - advantage of fused Silica is its uncommonly low Grüneisen coefficient Γ ($\Gamma \sim 0.035$)²²⁻²³ in correlation with its low Coefficient of Thermal Expansion (CTE ~ 5 10^{-7} K⁻¹). The practical consequence of this low Γ -

value is the very low shock-induced self-heating in the elastic domain of Silica, as compared to metals for instance, which removes the need for temperature compensation of the FBG signals. As an example, for a pressure level of about 4 GPa, the increase in temperature induced by the shock within the fiber is estimated to be around 1 K.²³

For most HE formulations, the detonation pressure is higher than 16 GPa and the fiber is thus destroyed within the detonation front. Based on this principle, CFBGs have been initially used for *in situ* continuous monitoring of detonation velocities. As the detonation wave travels through the CFBG, only the remaining part out of shock contributes to the Bragg spectrum. The amount of light reflected back by the CFBG is then declining progressively with time and is usually recorded with a high-speed photodetector (bandwidth up to several GHz) connected to a digital oscilloscope. The signal is then normalized to unity, transformed into shockwave front position with the help of a calibration curve and plotted versus time. Finally, detonation velocities are calculated by linear regression over selected time ranges of interest.⁶⁻¹⁰ On account of the derivative nature of the velocity parameter, the longer the sample, the better the uncertainty in velocity measurement. Best results were obtained along sustained detonations, for instance $\pm 0.6\%$ over 40 mm²⁴ and $\pm 0.3\%$ over 85 mm.⁸ Moreover, CFBGs used for velocity monitoring exhibit large spectral width (typ. 40 nm) and broad chirp (*e.g.* 0.3 to 0.6 nm/mm) with the aim to increase both the Signal-to-Noise Ratio (SNR) and the accuracy in position. The reflectivity of CFBG should be less than unity, *i.e.* the grating should not be saturated. Early calibration procedures involved destructive techniques such as fiber cut-back or laser fusion methods⁶, assuming that the FBG used for the shock loading experiment is identical to the calibrated one. A destructive analysis therefore relies on two main assumptions: (i) the Bragg grating photowriting process is reproducible, and (ii) the CFBG spectrum remains unchanged after integration into the HE material. In practice, the former assumption is realistic because most commercial FBGs are produced with the help of phase masks yielding high reproducibility. On the other hand, the latter assumption is actually not met in practice because the curing process has an impact over the CFBG spectrum due to permanent inhomogeneous strain after cure completion.

The authors had previously described a Non-Destructive Calibration (NDC) procedure involving Optical Frequency-Domain Reflectometry (OFDR) analysis that provides both reflection coefficient and spectral chirp (nm/mm) as a function of distance.²⁴ Based on these data a dedicated calibration curve is built for each CFBG inserted into the sample before the detonation experiment. Besides obvious cost considerations, this NDC procedure conveys better accuracy and reliability than usual destructive techniques because every CFBG is systematically calibrated before testing.

Besides pure velocity measurements, FBGs have also been investigated as *in situ* local pressure gauge in shock-loading experiments.^{11-15, 25} Lately, FBGs have been investigated as *in situ* continuous pressure sensor by several research teams.¹⁶⁻¹⁷ For impact stresses less than 9 GPa, usual Hooke relations may be used and the fiber is likely to survive the shock conditions

and provide information about its inner pressure distribution before it eventually breaks due to release waves and spalling effect. For impact stresses in the range [9 GPa - 16 GPa], the fiber part within the shockwave front may survive the shock conditions and provide complementary data in this range of pressure. However, the Hooke relations cannot be used in this stress range and a densification model must be used instead.²¹ Unlike CFBGs used for velocity monitoring, CFBGs investigated for continuous pressure monitoring exhibit narrower FWHM, in accordance with the required spectral resolution. It is worthwhile noticing that velocity measurement is still possible in this configuration as will be explained further on.

Based upon the Bragg equation (*i.e.* Eq. (1)), the Bragg wavelength depends on impact stress while the signal amplitude depends on the interaction length, as the reflection coefficient actually depends on grating length.¹⁹⁻²⁰ Real-time monitoring of the shock pressure has been firstly demonstrated with the use of an unbalanced Mach-Zehnder interferometer associated to 3 detectors connected to every output of a 3x3 coupler.^{11-12, 26} The Bragg wavelength shift was inferred from phase change (fringe counting) measured by a phase detection technique. Since the phase is calculated using an arctan function, phase unwrapping (or Lissajous plot) was undertaken for large phase shifts ($> 2\pi/3$) induced by the shock. The resolution in phase is expected to be as low as $2\pi/50$ (0.12 rad) with an optical path difference (OPD) of 3.1 mm which corresponds to a Bragg shift of 15 pm. The resolution in phase change depends on the OPD of the interferometer, itself limited by the coherence length of the light reflected by the FBG. Therefore, the spectral width of the FBG must be less than 0.43 nm for an OPD = 3.1 mm.

Van't Hof *et al.*¹¹ used a Westfalit explosive, commonly used in the mining industry, confined in a plastic box as a test charge, triggered by a high voltage igniter. This Ammonium Nitrate-based explosive material was chosen for its low detonation pressure (1 GPa) and low velocity (2 km/s). The authors proposed a calibration relationship linking pressure to Bragg wavelength shift based on Hugoniot data for Quartz.²⁷ They assumed a pure longitudinal compression state (along the shock direction, *i.e.* no radial strain) and disregarded both the elasto-optic effect (*i.e.* dependence of refractive index (RI) with respect to pressure) and the impedance mismatch between the explosive material and the fiber. A relative difference of 33 % between experimental (0.67 GPa) and expected (1 GPa) pressures is announced.

Deng *et al.*¹² used a one-stage gun projecting an Aluminum flyer over an Aluminum target attached to a container filled with water as experimental chamber for the FBG. The shock was then purely hydrostatic and the pressure range was restricted to [0, 1.4 GPa]. As a support for this experiment, the authors provided a 4th order-polynomial relationship linking the shock pressure to the Bragg wavelength shift that relies on the standard Bragg formula for sensitivity under hydrostatic interaction²⁸. The authors used a coefficient for index change with pressure deduced by Setchell²⁹ from planar shock experiments which is therefore unsuitable to hydrostatic configurations. Furthermore, impedance mismatch between Water

and Silica was not taken into account. A relative difference of 10 % between experimental and calculated pressures is announced by the authors.

Ravid *et al.*²⁵ and Shafir *et al.*¹⁵ made similar experiments with a gas gun launching a LEXAN impactor over PMMA targets with short-length (1 mm) FBGs embedded into it. The particle velocity at the rear facet of a gold-coated PMMA window was determined by the VISAR technique. The initial Bragg wavelength was 1552.5 nm. The signal reflected back by the FBG was recorded by a high-speed spectral analyzer composed of 5 add-drop filters in series (port #1 : @1546.1 nm to port #5 : @1554.1 nm) of central wavelength shifted by 1.6 nm, according to ITU grid. Each filter diverts the output wavelengths fitting into its spectral window to a detector and transfers all the other wavelengths to the next filter. The signal exiting the last filter is used as residue port and contains all upper wavelength contributions. Therefore, the spectrum is separated into 6 parts feeding 6 detectors. The bandwidth (FWHM) of each filter is 1.2 nm. The authors performed several experiments with different orientations for the FBG within the target (*i.e.* FBG perpendicular or parallel to shockwave front) and compared experimental and theoretical Bragg-to-pressure sensitivities for each. The authors proposed a simple relationship for the pressure-to-wavelength sensitivity that takes into account Gladstone-Dale relation for the photo-elastic effect. Furthermore, they assumed that the radial strain is null and that the FBG is purely longitudinally solicited. Based on these hypotheses, the authors also considered that the FBG does not experience axial strain when the shockfront is parallel to the fiber axis and that only photoelastic effects are still present. The authors then derived sensitivities of 9 nm/GPa (*i.e.* “red” shift) and -14 nm/GPa (*i.e.* “blue” shift) for parallel and perpendicular shockfront configurations respectively. Unfortunately, it is difficult to draw a conclusion about the accuracy of the model owing to the coarse spectral resolution (1.6 nm) of the add-drop based spectral analyzer. The authors tentatively provided a rough estimation of the experimental Bragg shift for a FBG oriented perpendicular to the shockwave front that is less than -6.4 nm for a calculated pressure of 0.48 GPa corresponding to an impact velocity of 296 m/s. A positive Bragg shift higher than 1.6 nm was observed for a FBG oriented parallel to the shockwave front, indicating that the sign effectively depends on fiber orientation.

Optomechanical models are evolving in complexity as experimentalists are gaining experimental feedback. The most recent experiments were performed at Los Alamos National Laboratory (LANL, USA) by G. Rodriguez *et al.*^{13,16}. They performed shock experiments with an explosive-driven water cell. The shock was then purely hydrostatic in nature. Both VISAR and PDV techniques were used for monitoring interface velocities at the front (Copper disc) and at the rear (PMMA window) of the water volume. The water pressure was estimated using Hugoniot relation²⁷ from shock speed (PDV) and particle velocity (VISAR) measurements. Rodriguez *et al.* investigated two different optical measurement approaches.

The first approach is based on the use of a Continuous-Wave (CW) ASE light source and a fiber-coupled spectrometer (12 outputs, channel spacing = 1.8 nm) associated to InGaAs photodetectors connected to digitizing oscilloscopes. Rodriguez *et al.* recorded a Bragg wavelength shift of -13.2 nm under an estimated pressure of 4.6 GPa thus corresponding to an average sensitivity of -2.87 nm/GPa with a fiber oriented parallel to the target axis.

The second one is less conventional as it uses an ultrafast mode-locked (ML) fiber laser source (repetition rate = 50 MHz) and a long run of SMF-28 fiber acting as a dispersive element and providing a wavelength-dependent delay time. The longer the fiber, the better the accuracy in both time and space domains. However, the delay time must be kept below the laser pulse period to prevent signals from overlapping onto each other, thus trading off accuracy against pressure range (or Bragg spectral range). According to the authors, the chromatic dispersion of the SMF-28 fiber is about 16.6 ps-nm⁻¹.km⁻¹, thus providing a relative time delay of about 0.67 ns/km over a spectral range of 40 nm (C-band). The use of a Faraday mirror at the extremity of the dispersive fiber enables to multiply the delay by a factor of 2 while cancelling undesirable additional delays due to Polarization-Mode-Dispersion (PMD) since light goes back and forth along the same guide. Finally, the great advantage of this second approach lies in the use of a single photodetector (high speed InGaAs photoreceiver, 12 GHz) coupled to a single channel of an ultra-high bandwidth oscilloscope (20 GHz). For each laser pulse, a time-domain waveform is recorded and transformed in the spectral-domain by the use of a single coefficient.

In a second experiment, Rodriguez *et al.*¹⁶ used a 100-MHz repetition rate ML laser as source, a 35-GHz photodetector and a 25-GHz bandwidth oscilloscope. They investigated the performance of their dispersive spectrometer with a FBG embedded into a polymer-bonded HE (PBX 9501), thermally ignited. In this situation, the state-of-stress inside the HE is considered as hydrostatic. Moreover, by contrast to previous reported experiments, the build-up dynamics of pressure was much slower (rise time ~ 25 μs). They observed a Bragg shift of about -5 nm for a maximum pressure of 1.2 GPa corresponding to an average sensitivity of -4.16 nm/GPa, close to the low-pressure hydrostatic sensitivity. Although the latter experiments were both performed in hydrostatic conditions, this experiment shows that the average sensitivity tends to decrease with increasing pressure, therefore witnessing a strong non-linearity in the pressure range [0, 4 GPa].

All these experimental results call for an improved model for the wavelength-to-pressure sensitivity of the FBG for each given shock conditions. In the following, we propose a model suitable to both hydrostatic and planar shock loading experiments that is confronted to experimental data.

III. OPTOMECHANICAL MODEL

As a basis for the model, we consider the symmetric planar shock loading configuration using a gas gun launching an Aluminum flyer over an Aluminum target. The main advantage of this configuration is the possibility to sustain a constant shock condition as a function of time/distance in the target material (*e.g.* 5.5 μs shock duration sustained over 30 mm for a shock velocity of 500 m/s and a target thickness of 55 mm). Sustained Bragg shifts are therefore also expected in the spectral domain. The stress of the sustained shock depends on both flyer velocity and material while its duration depends on both flyer and target geometries. The amplitude of shock stress may thus be adjusted by choosing several flyer velocities.

We first described the parameters used for the shock calculation and then we get into the details of the optomechanical model.

A. Equations of state (EOS) and determination of planar shock loading parameters

At the shock interface between flyer and target, the conservation of momentum and mass leads to usual Rankine-Hugoniot relations (Eq. (2, 3)):

$$\sigma = \rho_0 \cdot U \cdot u \quad (2)$$

$$\rho = \rho_0 \cdot U / (U - u) \quad (3)$$

where U is the velocity of the shockwave, u is the associated particle velocity, σ is the impact stress, ρ_0 and ρ are the density ambient and under shock respectively.

The densities of Aluminum 6061-T6 (temper 6) and fused Silica are 2.703 g/cm³ and 2.22 g/cm³ respectively.

The shockwave velocities U are related to particle velocities u by the nonlinear ($U-u$) Hugoniot relationships of the involved materials, written according to Steinberg notation³⁰ :

$$U_{Al}(km/s) = 5.33 + 1.37 \cdot u \quad [\text{Aluminum alloy 6061-T6}], \quad (4)$$

$$U_{SiO_2}(km/s) = 4.100 - 3.55 \cdot u + 18 \cdot (u/U_{SiO_2}) \cdot u \quad [\text{Fused Silica}], \quad (5)$$

The impact stress on Aluminum target is then expressed as:

$$\sigma_{Al} = 2.703 \cdot (5.33 + 1.37 \cdot u) \cdot u \quad (6)$$

Furthermore, particle velocity and stress are identical in both flyer and target at the shock interface. These values are obtained from the intersection of the target Hugoniot with the release isentrope of the flyer. For low stress values (less than several tens of GPa), the release isentrope is commonly approximated by the symmetrical (reflected) Hugoniot, as follows:

$$\sigma_{Al} = 2.703 \cdot (5.33 + 1.37 \cdot (V - u)) \cdot (V - u) \quad (7)$$

where V is the flyer velocity.

In our case, both flyer and target are made from the same material (6061-T6 Aluminum). This leads to the symmetrical impact condition for which the particle velocity at the interface equals to half the flyer velocity, *i.e.* $u = V/2$.

The impact stress σ is then obtained from the flyer velocity V by the following relation:

$$\sigma_{Al} = 1.3515 \cdot (5.33 + 0.685 \cdot V) \cdot V \quad (8)$$

In axisymmetrical conditions, the state-of-strain in an isotropic elastic material is described by Hooke laws:

$$\epsilon_z = \frac{\sigma_z}{E} - \nu \frac{\sigma_x}{E} - \nu \frac{\sigma_y}{E} = \frac{\sigma_z}{E} - 2\nu \frac{\sigma_r}{E} \quad (9a)$$

$$\epsilon_r = \frac{\sigma_r}{E} (1 - \nu) - \nu \frac{\sigma_z}{E} \quad (9b)$$

where ϵ_r and ϵ_z are the radial and longitudinal strains respectively, σ_r and σ_z are the radial and longitudinal stresses respectively, E is the modulus of elasticity (Young modulus) and ν is the Poisson coefficient. The longitudinal stress is oriented along the z -axis, the direction of shock and corresponds to the impact stress (Eq. (8)).

Under planar shock loading condition, the strain in the target is purely longitudinal (*i.e.* no radial strain), *i.e.* $\epsilon_r = 0$.

It follows from Eq. (9b) that the following relation always holds between radial and longitudinal stresses under planar shock loading configuration^{32,34}:

$$\sigma_r = \frac{\nu}{1-\nu} \cdot \sigma_z \quad (10)$$

We then introduce the longitudinal Young modulus E' associated to a planar wave propagation, as follows:

$$E' = \frac{\sigma_z}{\epsilon_z} = E \cdot \frac{1-\nu}{(1+\nu) \cdot (1-2\nu)} \quad (11)$$

In mechanical engineering, it is common to separate the state of stress into two components: (i) the spherical part (called pressure P) and (ii) the deviatoric part.

In axisymmetrical conditions, the pressure is written as follows:

$$P = (\sigma_z + 2 \cdot \sigma_r)/3 \quad (12)$$

In the elastic domain, the pressure may be written as a function of the impact stress by using Eq. (10), it yields:

$$P = \frac{\sigma_z}{3} \cdot \left(\frac{1+\nu}{1-\nu} \right) \quad (13)$$

In planar shock elastic loading condition, the major axis of the stress ellipsoid is thus oriented towards the z-axis (direction of shock).

In the case of Aluminum, the Young modulus is 69 GPa and the Poisson coefficient is close to 0.34.³¹ Then, one can find that $\sigma_z \sim 1.478 P$ and $\sigma_r \sim 0.761 P$.

In the case of Silica (Poisson coefficient $\sim 0,17$), one can find that $\sigma_z \sim 2.13 P$ and $\sigma_r \sim 0.436 P$. In planar shock loading, the impact stress in Silica is about twice the value of the pressure.

When the shear stress $\tau = (\sigma_z - \sigma_r)/2$ exceeds a threshold value $Y/2$ (Y is the so-called yield strength), the material enters into a plastic phase and the Eq. (9-13) are no longer valid.

The Hugoniot Elastic Limit (HEL) is the maximum longitudinal stress σ_z allowed in the elastic domain, before entering the plastic phase. From Eq. (10), we get:

$$HEL = Y \cdot \left(\frac{1-\nu}{1-2\nu} \right) \quad (14)$$

The yield strength Y is about 7 GPa for fused Silica from which we get the HEL value of 8.8 GPa.²¹⁻²²

Since the Y -value for aluminum alloy 6061-T6 increases with strain (*strain hardening effect*), we consider the zero-stress Y_0 -value ranging between 0.27 GPa and 0.31 GPa with 0.29 GPa as a medium standardized value.³¹ Eq. (14) yields the HEL value for 6061-T6 Aluminum at about 0.598 GPa³¹. From Eq. (13), the corresponding pressure is about 0.4 GPa.

For impact stress in excess of the HEL, the material is considered to behave hydrodynamically and the shear stress remains locked up to $\tau = Y/2$. The stress components are then very close to the pressure P (hydrodynamic approximation) as the stress ellipsoid is nearly spherical in shape.

In axisymmetrical conditions, we get for the stress components³⁴:

$$\sigma_z = P + \frac{2}{3}Y \quad (15a)$$

$$\sigma_r = P - \frac{1}{3}Y \quad (15b)$$

In practice, pressure P and impact stress σ_z are often mistaken for large value of impact stresses (several tens of GPa and more). However, for planar shock loading experiments in the range [0 – 4 GPa], P and σ_z should be distinguished as the Y -parameter of 6061-T6 Aluminum is not neglected.

Moreover, there is evidence from experiments with *in situ* Manganin or Carbon gauges³² about a strain hardening effect that manifests itself as an increase of the yield strength Y with increasing impact stress.³³⁻³⁵ In this paper, we consider the well-known Steinberg-Cochran-Guinan (SCG) model that expresses Y for 6061-T6 Aluminum as a function of pressure P and temperature T , as follows³⁶:

$$Y = Y_0 \cdot (1 + 125 \cdot \epsilon)^{0.1} \cdot \left[1 + 0.0652 \cdot \frac{P(\text{GPa})}{\eta^{1/3}} - 6.16 \cdot 10^{-4} \cdot \{T(K) - 300\} \right] \quad (16)$$

where η is the volume compression $\eta = V_0/V = \rho/\rho_0$ and ϵ is the plastic strain.

The volume compression η of 6061-T6 Aluminum may be estimated from Eq. (3) or from databases.²⁷ Under a shock pressure of 4 GPa, η is about 1.045 which gives a $\eta^{1/3}$ value of 1.015. Consequently, the influence of volume compression in Eq. (16) is about 1.5 % and may be neglected for pressure values in the range [0 – 4 GPa].

Moreover, the shock-induced heating of a material under hydrostatic pressure may be estimated from the calculation of the Hugoniot temperature in the shockfront²³:

$$T_H \approx T_0 \cdot \exp(\Gamma \cdot \eta) \approx T_0 \cdot \exp(3 \cdot \Gamma \cdot \epsilon) \quad (17)$$

where Γ is the Grüneisen coefficient and the volume compression η is expressed as a function of the plastic strain ϵ considered as hydrostatic :

$$\epsilon = \frac{P}{E} \cdot (1 - 2\nu) \quad (18)$$

Considering the case of Aluminum ($\Gamma_{Al} \sim 2.14$)³⁷, the hydrostatic (plastic) strain is about 1.86 % under a pressure of 4 GPa. The increase in temperature due to the shock is estimated to be about 37 K for a given pressure of 4 GPa. Since it accounts for only 2 % in the Y -value in Eq. (16), the temperature contribution is also neglected.

Considering the case of Silica ($\Gamma_{\text{SiO}_2} \sim 0.035$)²²⁻²³, the hydrostatic (elastic) strain is about 3.67 % under a pressure of 4 GPa. The increase in temperature of fused silica due to shock self-heating is estimated around 1.15 K in the same pressure range which may be neglected as well.

Based upon these remarks, Eq. (16) simplifies as follows:

$$Y \approx Y_0 \cdot \left(1 + 125 \cdot \frac{P}{E} \cdot (1 - 2\nu)\right)^{0.1} \cdot [1 + 0.064 \cdot P(\text{GPa})] \quad (19)$$

The table 1 shows up all the constitutive parameters for 6061-T6 Aluminum and fused Silica.

It is interesting to notice that the shock impedances of 6061-T6 Aluminum and fused Silica differ from more than 35 % in the elastic domain. In the hydrodynamic domain, the bulk sound speed of shock is 5.33 km/s, the shock impedance of Aluminum is smaller in the hydrodynamic domain than in the elastic domain and better matches that of Silica.

TABLE I. Constitutive parameters of 6061-T6 aluminum and fused silica.

	6061-T6 Al	Ref.	Fused Silica	Ref.
Young modulus E (GPa)	69	Ref. 31, 36	72	Ref. 57
Young modulus E' (longitudinal, GPa)	97	Ref. 31, 36	77.6	Ref. 57
Poisson coefficient ν (dimensionless)	0.34	Ref. 38	0.17	Ref. 47, 53
HEL (GPa)	0.598	Ref. 36	8.8	Ref. 22
Y_0 (GPa)	0.29	Ref. 36	7	Ref. 22
Gruneisen coefficient Γ (dimensionless)	2.14	Ref. 37	0.035	Ref. 23
Density ρ (g/cm ³)	2.703	Ref. 37	2.22	Ref. 57
Shock speed C_0 (bulk, km/s)	5.33	Ref. 37	4.10	Ref. 27
Sound velocity C_L (longitudinal, km/s)	6.40	Ref. 27	5.96	Ref. 27
Hugoniot parameter S_1	1.37	Ref. 37	-3.55	Ref. 31
Hugoniot parameter S_2	0		18	Ref. 31
Shock impedance Z (elastic domain, kg.mm ⁻² .s ⁻¹)	14.4	Ref. 27	9.1	Ref. 27

B. Determination of aluminum-to-silica coupling parameter

The previous section describes the state-of-stress of both flyer and target during planar shock loadings. We then consider the application of the stress distribution within the 6061-T6 Aluminum target onto a silica fiber, placed along the target axis, oriented longitudinally (Fig. 1). Since the fiber diameter is small (~ 150 micrometers with a polyimide coating), and the values of Young modulus of both 6061-T6 Aluminum and fused Silica are close (Table I), we assume that the fiber insertion does not significantly change the stress distribution within the target. However, the shock impedances of both materials are not equivalent (see Table I) and thus the pressure applied to the fiber is expected to be different from that within the target.

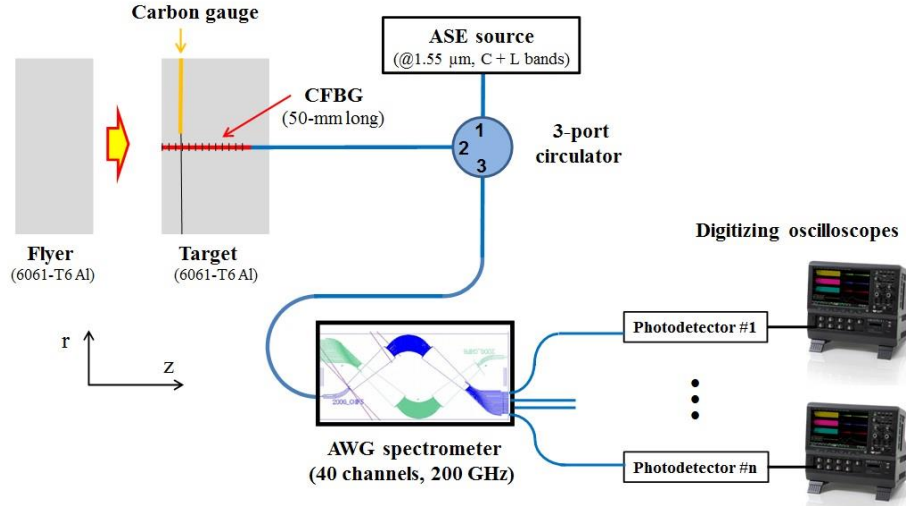


FIG. 1. Description of the experimental setup.

Usual one-dimensional analysis involves the calculation of stresses in 6061-T6 Al and Silica using the Hugoniot relations Eq. (4-5) injected into Eq. (2) with respect to the particle velocity, deduced from flyer velocity. The stress value at the Al-SiO₂ interface is obtained by the intersection of the Hugoniot of Silica with the reflected Hugoniot of 6061-T6 Al (*i.e.* Eq. (7)). The coupling coefficient K is defined as the pressure ratio between fiber and target:

$$K_{Al-SiO_2} = \frac{P_{SiO_2}}{P_{Al}} \quad (20)$$

At first glance, an order of magnitude of the Aluminum-to-Silica coupling coefficient is obtained from the usual relationship:

$$K_{Al-SiO_2} \approx \frac{2 \cdot Z_{SiO_2}}{Z_{SiO_2} + Z_{Al}} \quad (21)$$

where Z_{SiO_2} and Z_{Al} are the shock impedances of Aluminum and Silica respectively.

This 1D analysis provides a rough estimation (77 %) of the coupling coefficient for the elastic domain of 6061-T6 aluminum. A Finite-Element Modeling (FEM) of both flyer and target has been undertaken in a 2D axisymmetric configuration and accounts for elastoplasticity (SCG model³⁶) of the 6061-T6 Aluminum material as well. The stress distributions within target and fiber were determined for several impact velocities V using the OURANOS hydrodynamic code.

Two 2D calculations have been carried out with the aim to estimate the Aluminum-to-Silica coupling coefficient K with respect to flyer speed. A first 2D calculation (unrealistic) has been carried out without epoxy and a second one (realistic) was performed with the epoxy layer placed in-between target and fiber in order to analyze the influence of this interface on the pressure transfer from Aluminum and Silica.

Fig. 2 shows typical results obtained for an impact velocity of 0.5 km/s with the OURANOS hydrodynamic code displaying the pressure distributions along fiber axis and in the Aluminum target nearby. In Aluminum, the elastic precursor travels faster ($C_L \sim 6.4$ km/s) than the plastic shock ($C_p \sim 5.7$ km/s). Fig. 2a depicts the pressure distributions obtained when both materials are directly in contact. Fig. 2b depicts the pressure distributions obtained when an epoxy layer (Araldur AY103) is placed in between the Aluminum target and the Silica fiber. Some calculations were performed for several impact velocities V and the 2D stress ratio of sustained shock pressures P_{SiO_2}/P_{Al} has been plotted in Fig. 3 with respect to impact stress (according to Eq. (8)). Without epoxy the parameter K_{Al-SiO_2} increases linearly with stress until reaching a maximum value of about 0.96 around 3.2 GPa on account of the decrease of the impedance of 6061-T6 Al (decrease of shock speed).

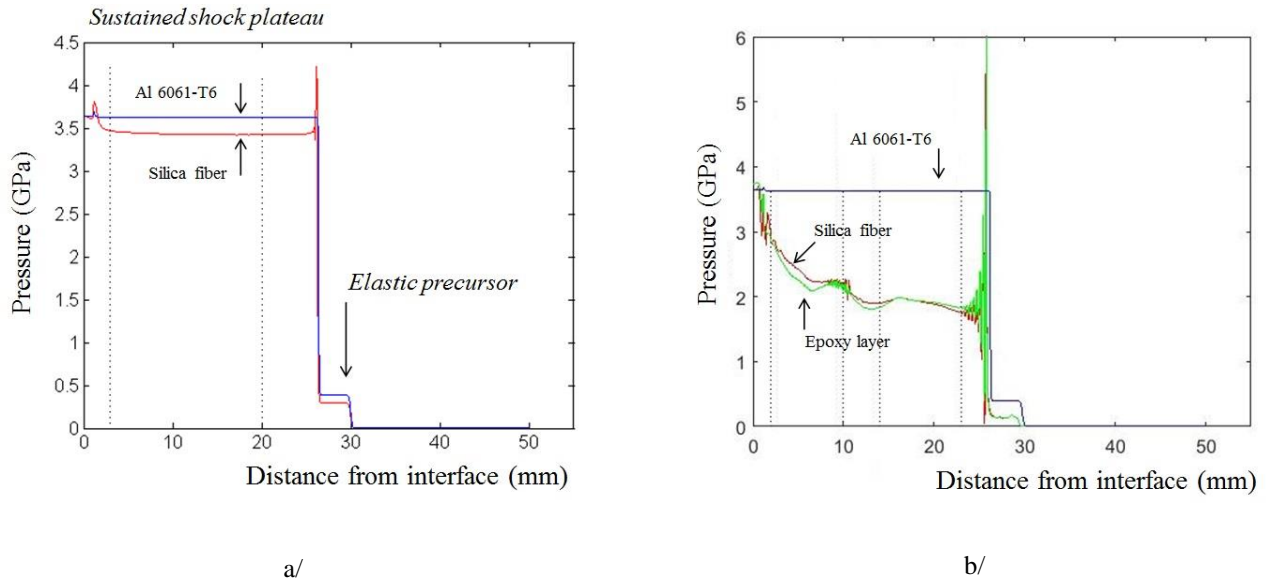


FIG. 2. Pressure distributions in the 6061-T6 Al target (close to axis) and in fiber (located along the axis), as calculated by the hydrodynamic/elastoplastic OURANOS hydrodynamic code ($V = 0.5$ km/s). Calculations without epoxy (a/left) and with epoxy b/(right). The pressure within Aluminum due to the elastic precursor shockwave is 0.4 GPa ($HEL = 0.598$ GPa) while the sustained shock pressure depends on flyer velocity.

An empirical relation is found that fits well the calculated data in the range $[0 - 4$ GPa] of pressure:

$$K_{Al-SiO_2}(P_{Al}) = 0.766 + 0.092 \cdot \frac{P_{Al}}{(1+0.06 \cdot P_{Al}^2)} \quad , \quad (22)$$

Regarding the elastic precursor, the coupling coefficient calculated by the hydrodynamic code is about 0.77, similar to the analytic calculation (Eq (21)).

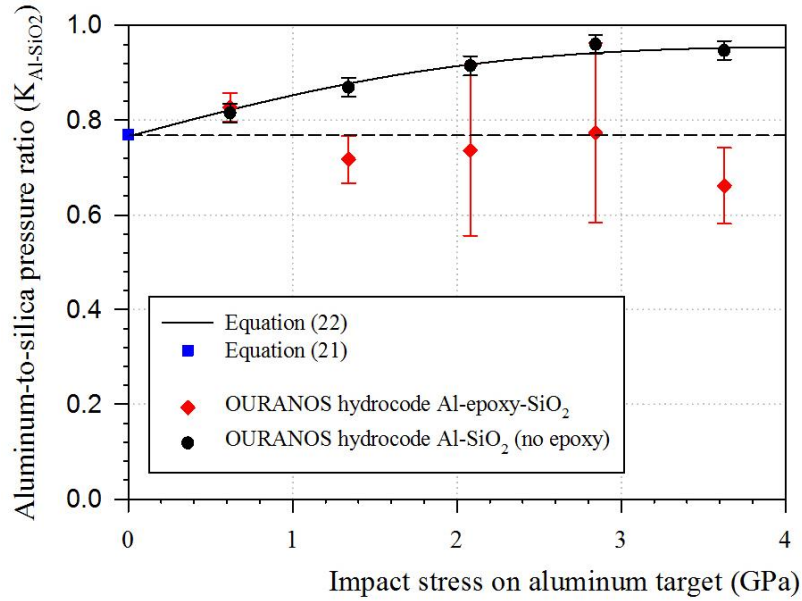


FIG. 3. Ratio of sustained shock pressures P_{SiO_2}/P_{Al} (coupling coefficient K_{Al-SiO_2}) with respect to impact stress close to target axis, as calculated by the OURANOS hydrodynamic code over the sustained shock plateau (according to figure 2).

In presence of an epoxy layer, the coupling coefficient K_{Al-SiO_2} from Aluminum to Silica is roughly constant at a value around 0.78 ± 0.05 within the pressure range of interest. In spite of great attention paid in increasing the mesh resolution (node interval below 10 micrometers) within the epoxy layer, the pressure on the sustained part of the shock was poorly determined within the fiber, on account of the multiple shock reflections occurring within the epoxy layer. Indeed, the shockwave is no more directly coupled to the Silica fiber but reflected instead within the epoxy layer placed in between Aluminum and Silica of greater shock impedances.

These calculations lead to the conclusion that the epoxy layer has a significant impact on the pressure transfer from the Aluminum target to the Silica fiber. When the Silica fiber is placed directly in contact to Aluminum, the coupling coefficient increases as the shock impedance of Aluminum get closer to that of Silica. In practice however, epoxy is required both for practical handling and to eliminate air bubbles as well. Therefore, we consider a constant pressure coupling coefficient in the rest of the paper due to presence of epoxy. Furthermore, the numerical modelings show that the sustained shock part is less well-defined in presence of epoxy which is likely to have an impact on the experimental dispersion of the Bragg data.

C. Optomechanical model for Bragg grating strain gauge

Previous developments provide the necessary relationships linking the state-of-stress in the fiber to that in the target used for planar shock loading experiments. In this third part, we get into the details of the Bragg grating shift under stress transferred from the aluminum target to the embedded Silica fiber.

1. Constitutive equations

a. Bragg wavelength

Differentiating Eq. (1) we get:

$$\frac{d\lambda_B}{\lambda_B} = \frac{d\Lambda}{\Lambda} + \frac{dn}{n} \quad (23)$$

The first term of Eq. (23) is the longitudinal strain ε_z and the second term is due to elasto-optics and density change. The first and second terms of Eq. (23) are of opposite sign, refractive index (RI) change counterbalancing the effect of mechanical compression. The strain-induced RI change is related to the strain *via* the following relation³⁸:

$$\Delta\left(\frac{1}{n_i^2}\right) = -2 \cdot \frac{\Delta n_i}{n_i^3} = \sum_j p_{ij} \cdot \varepsilon_j \quad (24)$$

where p_{ij} is the strain-optic tensor composed of photo-elastic constants of fused Silica³⁹, also called elasto-optic or Pockels' coefficients. As silica is a homogeneous isotropic material, the strain-tensor is symmetric and only p_{11} , p_{12} and p_{44} components are considered, with $p_{44} = (p_{11} - p_{12})/2$.

Eq. (24) holds for “small” strain values, *i.e.* of several percents. Submitted to an intense planar shock or hydrostatic pressure loading, silica may undergo large compressive strains and a deviation from Eq. (24) is likely to happen.

Vedam and Srinivasan⁴⁰ proposed the following relation for large strains:

$$\Delta\left(\frac{1}{n_i^2}\right) = -2 \cdot \frac{\Delta n_i}{n_i^3} = \sum_j p_{ij} \cdot \varepsilon_j + \sum_j p'_{ij} \cdot \varepsilon_j^2 \quad (25)$$

To the best of our knowledge, there is no published data describing second-order photoelastic p'_{ij} Pockels coefficients of Silica fibers. Since the hydrostatic strain in Silica is approximately -0.036 (-3.6 %) under a hydrostatic pressure of 4 GPa, one may estimate the square of it (ε^2) at about $1.3 \cdot 10^{-3}$. If we assume that the second-order Pockels coefficients p'_{ij} are of same order of magnitude as p_{ij} , then the deviation from linearity should be about $\varepsilon^2/\varepsilon = \varepsilon \sim 3\%$ to 4% , which is of the same order of magnitude as the uncertainty in Bragg wavelength with the current set-up.

Therefore, we make the assumption in the following part of this paper that Eq. (24) is still valid within the pressure range [0 – 4 GPa], disregarding any second-order contribution.

The shift in Bragg wavelength λ_B is then given by²⁰:

$$\frac{\Delta\lambda_B}{\lambda_B} = \varepsilon_z - \frac{n^2}{2} \cdot [\varepsilon_r \cdot (p_{11} + p_{12}) + \varepsilon_z \cdot p_{12}] \quad (26)$$

where n is the effective index of the LP₀₁ mode propagating in the fiber core ($n \sim 1.47$), ε_z and ε_r are the strains as given by Eq. (9a) and Eq. (9b) respectively.

As light propagates along the z-axis, the electric field vector is radially-oriented (along $r = x = y$). The p_{11} coefficient corresponds to a change in RI along a direction collinear to the applied strain while the p_{12} coefficient corresponds to a change in RI in a direction perpendicular to the applied strain.

Under the application of hydrostatic pressure, the shift in Bragg wavelength becomes:

$$\frac{\Delta\lambda_B}{\lambda_B} = (1 - p_h) \cdot \varepsilon \quad (27)$$

where ε is the strain given by Eq. (18) and p_h is the photo-elastic constant in hydrostatic configuration given by:

$$p_h = \frac{n^2}{2} \cdot (p_{11} + 2 \cdot p_{12}) \quad (28)$$

For instance, Xu *et al.*²⁸ reported a relative Bragg sensitivity of $1.98 \cdot 10^{-6} \text{ GPa}^{-1}$ leading to an absolute Bragg sensitivity of -3.04 nm/GPa (@1530 nm).

Similarly, Morey *et al.*⁴¹ obtained a relative Bragg sensitivity of $-2.22 \cdot 10^{-6} \text{ GPa}^{-1}$ (@1304 nm) leading to an absolute sensitivity of -2.89 nm/GPa (@1304 nm) and a calculated sensitivity of -3.44 nm/GPa (@1550 nm). Both fibers were Germanosilicate-based and had their coating removed before testing.

Conversely, under the application of a longitudinal strain (oriented along the z-axis), Eq. (26) becomes:

$$\frac{\Delta\lambda_B}{\lambda_B} = (1 - p_e) \cdot \varepsilon_z \quad (29)$$

where p_e is the photo-elastic constant that rules the Bragg grating sensitivity under longitudinal strain, as follows:

$$p_e = \frac{n^2}{2} \cdot [p_{12} \cdot (1 - \nu_{SiO2}) - p_{11} \cdot \nu_{SiO2}] \quad (30)$$

The p_e coefficient is usually ranging between 0.2 to 0.22 at 1550 nm in Germanosilicate fibers depending on GeO_2 concentration in the core (the larger the concentration, the greater the p_e -value).^{20,42} For instance, Julich *et al.*⁴² performed strain measurements on FBG photowritten in different fiber types. For a SMF-28 fiber (~ 4 %wt GeO_2 in the core), they obtained a p_e -value of 0.205 ± 0.004 (@1530 nm).

b. Photoelastic constants p_{11} and p_{12}

Early developments about Optical Fiber Sensors (OFS) were essentially dedicated on birefringence change under stress, that is the difference $p_{11} - p_{12}$ (also equivalent to $2p_{44}$).⁴³⁻⁴⁶ Moreover, most optical sources were available in the visible range at this time and as a consequence of all this, few data have been published about Pockels coefficients of Silica in the near infra-red (NIR) range, especially in the third telecommunication window largely used nowadays (@1550 nm).

Since p_{11} and p_{12} values are composition-dependent, the most pertinent values are obtained from the analysis of singlemode fibers instead of bulk glass. For instance, Bertholds and Dandliker⁴⁷ obtained the following values: $p_{11} \sim 0.113$ and $p_{12} \sim 0.252$ for a pure silica-core singlemode fiber (with a boron-doped cladding) at 632.8 nm (He-Ne laser). These values are still used extensively although today's applications mainly involve the use of Germanosilicate fibers operating in the NIR domain (@1550 nm).

The measurement of both p_h and p_e coefficients (Eq. (27) and Eq. (29)) provides a matrix system making it possible to discriminate p_{11} and p_{12} . However, the relative accuracy must be high enough (*i.e.* less than 0.1 %) since the matrix inversion always leads to a degradation of the accuracy owing to the propagation of uncertainties.

A recent measurement of p_{11} and p_{12} coefficients at the wavelength of 1550 nm is due to P. Dragic *et al.*⁴⁸ with both commercial Z-fiber (Sumitomo) and custom-made Aluminosilicate-based fiber. The Z-fiber is a pure Silica-core fiber with a Fluor-doped cladding. The authors have designed two separate optical setups. A first setup was made of a fiber laser incorporating the fiber under test, strained using a translation stage. The authors recorded the change in the Free Spectral Range (FSR) as a function of strain and thus got an accurate value for the photoelastic constant p_e with a relative uncertainty of $\sim 10^{-4}$. A second setup was made of a linear twisted strand of fiber associated to a polarized light source at the input and a Glan-Taylor polarizing prism at the output. The authors recorded the polarization state at the output as a function of fiber twist thus leading to an estimation of $p_{11} - p_{12}$ with a relative uncertainty of $\sim 4 \cdot 10^{-3}$. Solving for p_{11} and p_{12} led to $p_{11} = 0.226 \pm 0.012$ and $p_{12} = 0.098 \pm 0.004$ respectively for the Z-fiber.

Since Dragic's⁴⁸ and Bertholds's⁴⁷ teams both investigated pure silica-core fibers, the difference in photoelastic constants may be attributed to wavelength dependence. As a support to this observation, it is worthwhile noticing that Namihara⁴⁶

reported unusually low values for the stress-optic coefficient C (in mm^2/kg) of Germanosilicate fibers in the NIR domain with respect to expected values based on the model proposed by Sinha⁴³, from experimental data in the visible range. The relative C coefficient ($C = C_1 - C_2$) is actually proportional to the difference $p_{12} - p_{11}$. Namihara⁴⁶ reported C -values of $3.03 \cdot 10^{-5} \text{ mm}^2/\text{kg}$ and $3.34 \cdot 10^{-5} \text{ mm}^2/\text{kg}$ at $1.58 \mu\text{m}$ and $0.632 \mu\text{m}$ respectively, showing a wavelength dependence of -9.3% .

The p_e -value for the Z-fiber is then estimated of about 0.19, based upon the data of Dragic *et al.*⁴⁸ This value is smaller than those reported for GeO_2 -doped fibers, in accordance with the observations of Julich *et al.*⁴²

Let us assume that the wavelength dependence for the Pockels coefficients observed by Namihara⁴⁶ for Germanosilicate fibers is of the same order as for pure silica core fibers. Applying this correction to the coefficients obtained at $0.632 \mu\text{m}$ by Bertholds⁴⁷ yields the following value (projected at $1.58 \mu\text{m}$) for $p_{12} - p_{11} \sim 0.126$. The value proposed by Dragic *et al.*⁴⁸ ($p_{12} - p_{11} \sim 0.128$) is thus in accordance with the projected value calculated from the data from Bertholds⁴⁷ (0.126), thus increasing the confidence in their result.

In our study, we used a ZBL ClearcurveTM bend-insensitive fiber (Corning). The cross section of this fiber shows up three concentric zones. The first zone is the core doped with GeO_2 ($\sim 0.4 \%$ wt, $\sim 8 \mu\text{m}$ in diameter) that raises the index. The second zone is a transition zone often pure-Silica based. Finally, the third zone (“trench”) incorporates Fluor or a special nano-engineered glass⁴⁹ that lowers the index. The inner diameter is between $6.5 \mu\text{m}$ and $11 \mu\text{m}$ depending on the index trench (the larger the index, the greater the radius). Since the germanium concentration is comparatively small to usual singlemode fiber (*e.g.* SMF28) and a significant part of the LP_{01} mode actually spreads in the pure-Silica core region, we assume that the proper values for p_{11} and p_{12} at 1550 nm should be close to that obtained by Dragic *et al.*⁴⁸ with a Z-fiber.

Finally, it is also interesting to note that the values of photoelastic coefficients actually depend on the refractive index *via* a Lorenz-Lorenz parameter $(n^2 - 1)^2/n^4$, and thus on density change induced by compaction under pressure⁵⁰. Any change in the linear Pockels coefficient due to pressure-dependency would correspond to a second-order contribution (p'_{ij}), as described by Eq (25). However, in the pressure range of interest [$0 - 4 \text{ GPa}$], we made the assumption that the second-order contribution to the photo-elastic change under strain might be disregarded and the Pockels coefficient does not change significantly under the pressure range of interest of this study.

c. Refractive index n

Conversely, the refractive index n is highly stress-dependent according to pressure-induced density change as described by the usual Gladstone-Dale (GD) model⁵¹:

$$\frac{d\rho}{\rho} = \frac{dn}{(n-1)} \quad (31)$$

From the work of Arndt and Stöffler⁵² using a sodium lamp, we get the following first-order GD-type relation for fused Silica (Suprasil) under hydrostatic pressure:

$$n \approx 0.977 + 0.218 \cdot \rho (g/cm^3) \quad (32)$$

The density change of fused Silica under hydrostatic pressure as compiled from different authors by Zha *et al.*⁵³ shows a slope of approximately 0.072 GPa⁻¹. A second-order relation may thus be obtained for the RI change from the data provided by Zha *et al.*⁵³:

$$n \approx 1.042 + 0.216 \cdot \rho - 0.0129 \cdot \rho^2 \quad (33)$$

Cohen and Roy^{54,55} found that the RI of fused Silica exhibits a quasi linear behavior in the range [2 - 16 GPa] and so does the density^{53,22}. The anomalous behavior of the RI in the range [0 – 2 GPa] should be put in perspective with the evolution of the Young modulus^{56,57}, commonly attributed to the compaction of the open oxygen network into a denser configuration.

Several authors^{51,56} argued that the GD model is not suitable for fused Silica and proposed a correction factor to account for experimental deviation. Furthermore, in the elastic domain of Silica (*i.e.* impact stress less than its HEL value), the state of stress is highly dependent on the shock loading configuration and so does the refractive index. For instance, Barker and Hollenbach⁵⁶ and Dandekar⁵¹ performed planar shock loading experiments on Silica-glass based targets and investigated the evolution of RI under shock using a He-Ne laser (@632.8 nm) based interferometric setup to measure the interface velocities.

Dandekar⁵¹ reported a measured index-to-shock stress $\Delta n/\Delta\sigma$ coefficient of 0.0056 GPa⁻¹ (@514.5 nm). Setchell²⁹ analyzed the Doppler data obtained by Barker and Hollenbach⁵⁶ and reported a graph displaying the change of RI vs the impact stress (erroneously called "pressure" in the article on account on planar impact loading). From this graph, we get the following relationship for the RI change vs impact stress:

$$\Delta n \approx 4.6 \cdot 10^{-3} \sigma_z + 8.6 \cdot 10^{-4} \sigma_z^2 - 5 \cdot 10^{-5} \sigma_z^3 \quad (34)$$

Vedam⁵⁸ performed laser interferometric velocity measurements (@589.3 nm) on hydrostatically-stressed Suprasil glass pellets and reported index-to-pressure $\Delta n/\Delta P$ coefficients of 0.0092 GPa⁻¹.

Finally, Zha *et al.*⁵³ performed high pressure studies on Silica Herasil polished platelets inserted inside diamond cells illuminated by laser light. The wavelength and laser type are not given. They recorded the spectral shifts of Brillouin

scattered light as a function of internal pressure measured by the ruby fluorescence technique. They also determined the variation of RI with pressure using a refractometric technique (Fig. 4). From Brillouin shifts and RI measurements, Zha *et al.*⁵³ obtained transverse and longitudinal sound velocities and Poisson ratios of Silica as a function of pressure.

As a rule of thumb, the RI-to-hydrostatic pressure $\Delta n/\Delta P$ coefficient is twice that of RI-to-shock stress $\Delta n/\Delta \sigma$ coefficient on account of the different state of stress in both configurations. Referring to Eq. (13), the pressure value in Silica is about the half of the impact stress in planar shock loading. The difference between reported RI change-to-stress sensitivities is attributed to the different stress distributions for both planar and hydrostatic configurations.

In this work, we consider that the silica fiber is hydrostatically stressed for impact stress in excess of the HEL_{Al} , according to the hydrodynamic approximation for the Aluminum material (Eq. (15)). For impact stress less than HEL_{Al} , this assumption is not correct but the difference in RI estimation was considered as negligible (on account of the low HEL value).

In the following, we used the RI-to pressure relation obtained by Zha *et al.*⁵³:

$$n = 1.459 + 1.147 \cdot 10^{-2} \cdot P - 6.68 \cdot 10^{-5} \cdot P^2 \quad (35)$$

where P is the pressure in GPa.

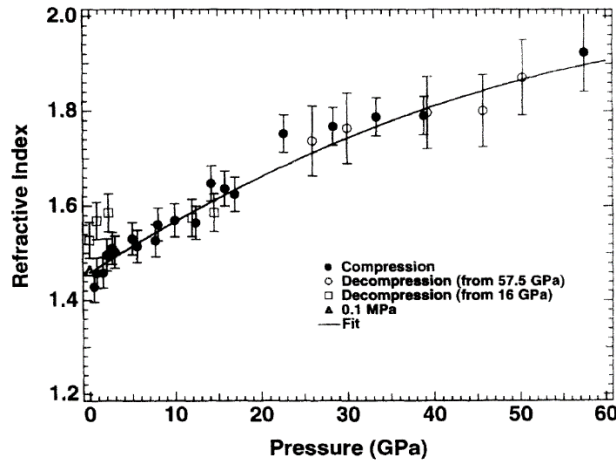


FIG. 4. Evolution of the refractive index for fused silica with respect to hydrostatic pressure (from Ref. 53)

d. Young modulus E_{SiO2}

Among few planar shock loading experiments performed with fused Silica as flyer/target material, the pioneering work of Barker and Hollenbach⁵⁶ is often cited. Using a laser interferometric velocity setup (earlier to VISAR technique⁴), they were able to determine both particle and shockwave velocities as a function of flyer velocity. From these measurements, they were able to calculate the stress (from Eq. (2)) and the longitudinal strain ($\epsilon_z = u/U$, as obtained from Eq. (3)). The

longitudinal Young modulus E' (sometimes also noted C_{11}) is then determined from the stress/strain ratio. Finally, the Young modulus E may be retrieved from the longitudinal Young modulus by applying Eq. (11).

Barker and Hollenbach⁵⁶ provided a fourth-order polynomial relation for the stress σ as a function of compressive strain ε_z , useful in the range [0, 18%]:

$$\sigma(\varepsilon_z) = 77.6 \cdot \varepsilon_z - 415.9 \cdot \varepsilon_z^2 + 3034 \cdot \varepsilon_z^3 - 6926 \cdot \varepsilon_z^4 \quad (36)$$

Differentiating with respect to strain, we get the longitudinal Young modulus E' :

$$E'(\varepsilon_z) = 77.6 - 831.8 \cdot \varepsilon_z + 9102 \cdot \varepsilon_z^2 - 27704 \cdot \varepsilon_z^3 \quad (37)$$

To be useful, this relation should better be expressed as a function of stress which is the input value in our study. Then, we propose a fourth-order fitting equation of E' vs σ , as:

$$E'(\sigma_z) = 77.6 - 11.2 \cdot \sigma_z + 1.035 \cdot \sigma_z^2 + 0.143 \cdot \sigma_z^3 - 0.016 \cdot \sigma_z^4 \quad (38)$$

The longitudinal Young modulus E' reaches a minimum of approximately 54 GPa under an impact stress of 4 GPa.

As pointed by Kondo *et al.*⁵⁷, the evolution of E' under planar shock loading as deduced from Barker's experiment is notably different from that obtained under hydrostatic conditions. Kondo *et al.*⁵⁷ performed ultrasonic (US) velocity measurements over glass samples immersed into a fluid under pressure, measured using a Manganin gauge up to 3 GPa (30 kbar). The authors measured the velocities of shear and longitudinal waves as well as the evolution of the sample length under pressure, and calculated the longitudinal modulus E' , plotted as a function of pressure (Fig. 5). They found that the longitudinal Young modulus E' reaches a minimum of about 62 GPa under an hydrostatic pressure of 2.33 GPa.

Kondo *et al.*⁵⁷ proposed a second-order polynomial relation for the longitudinal Young modulus E' (in GPa) as a function of hydrostatic pressure P (in GPa), as follows:

$$E'(P) = 62.25 + 4.15 \cdot (P - 2.33)^2 \quad (39)$$

for $1.3 \text{ GPa} < P < 3 \text{ GPa}$.

Based on the data obtained by Kondo *et al.*⁵⁷, we propose another relationship applicable in the range [0 – 3 GPa]:

$$E'(P) = 78 - 9.05 \cdot P - 1.29 \cdot P^2 + 1.2 \cdot P^3 - 0.094 \cdot P^4 \quad (40)$$

This equation is also plotted on fig. 5 and overlaps that of Kondo *et al.*⁵⁷ very well. The behavior of the Young modulus E' as reported by Kondo *et al.*⁵⁷ is also confirmed by Meade and Jeanloz⁵⁹. However, in the absence of accurate experimental data in the range [3 – 4 GPa], the values are only indicative up to 4 GPa.

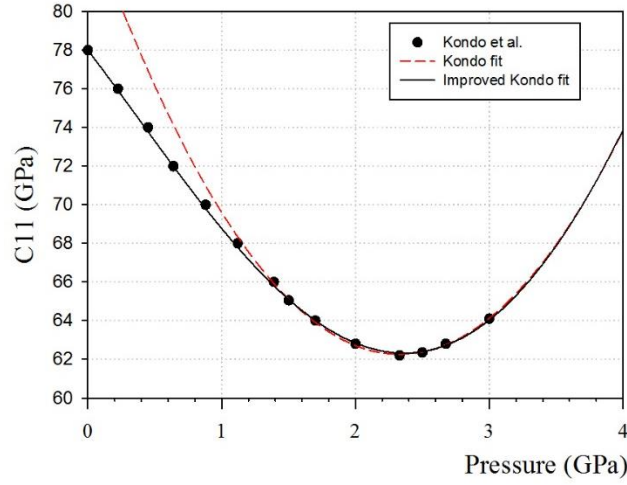


FIG. 5. Evolution of the longitudinal Young modulus E' of a Silica glass material as a function of hydrostatic pressure (data from Ref. 57) and best fit in the pressure range [0 – 3 GPa]

e. Poisson ratios ν_{Al} and ν_{SiO_2}

According to Glushak³³, the Poisson coefficient of Aluminum may be considered as constant with respect to pressure. For 6061-T6 Aluminum, we consider the following value $\nu_{Al} = 0.34$.

Liu *et al.*⁶⁰ gave the evolution of the Poisson coefficient of Silica as a function of hydrostatic pressure and found a slope of approximately -0.01 GPa^{-1} in the range [0 – 0.5 GPa].

Finally, Zha *et al.*⁵³ obtained the pressure dependence of the Poisson coefficient of Silica glass as a function of pressure by Brillouin shift measurements (Fig. 6). The pressure dependence of the Poisson coefficient of Silica ν_{SiO_2} is to be compared to that of the Young modulus. The Poisson coefficient of Silica decreases with the applied pressure until reaching a minimum value at 2 GPa, then it increases again for higher pressure. It eventually reaches a plateau value around 0.31 as the pressure exceeds the HEL value of Silica and permanent compression occurs up to a density change of -20% ⁶⁰.

We propose a fitting relation (Fig. 6) based upon these results in the range [0 – 9 GPa], that takes into account the first-order slope found by Liu *et al.*⁶⁰ (Eq. (41)):

$$\nu_{SiO_2}(P) \approx 0.17 - 0.01 \cdot P + 4 \cdot 10^{-3} \cdot P^2 - 1.6 \cdot 10^{-4} \cdot P^3 \quad (41)$$

Since a large uncertainty is associated to the determination of the Poisson's ratios from acoustic velocities ($\pm 6\%$), the uncertainty associated to the coefficients of fit is of same order of magnitude.

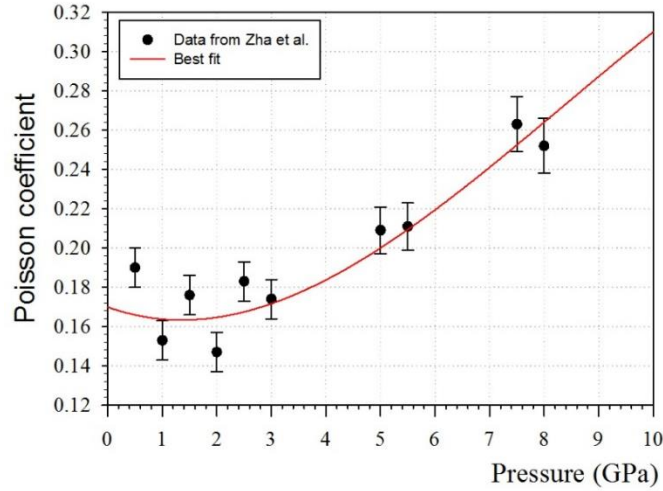


FIG. 6. Evolution of the Poisson coefficient of Silica as a function of hydrostatic pressure (data from Ref. 53) and best fit in the pressure range [0 – 9 GPa]

2. Generalized Bragg model for elastic and hydrodynamic target behavior

Eq. (25) and Eq. (29) provide a way to calculate the Bragg wavelength shift as a function of state of strain (ϵ_z, ϵ_r) applied onto the fiber, embedded into the target, calculated using Eq. (9a) and Eq. (9b) respectively.

For variable impact stress σ_{Al} on 6061-T6 Al target depending on the flyer velocity V (Eq. (8)), the stress σ_{SiO_2} coupled to the fiber is estimated using a fixed coupling coefficient value of 0.78. In the following, the pressure range of investigation was [0 – 4 GPa].

6061-T6 Aluminum is a common material for shock loading experiments since a lot of data have been gathered on this material for several decades^{27,31,36,37}. In conjunction with fused Silica fiber as pressure gauge, such material provides the advantage of a close shock impedance matching between the sustained plastic shockwave with the elastic shockwave traveling in Silica. However, 6061-T6 Aluminum shows an elasto-plastic transition for impact strengths in excess of its HEL value that further complicates this analysis. On the other hand, Silica is considered to behave elastically in the pressure range of [0- 4 GPa] so that Hooke laws apply for this material.

Based on constitutive equations previously stated, the Poisson ratio ν_{SiO_2} and longitudinal Young modulus E'_{SiO_2} of Silica are obtained using Eq. (41) and Eq. (40) respectively. The linear Young modulus of Silica E is then calculated from the value of the longitudinal Young modulus and Poisson's ratio, using Eq. (11).

We then consider two distinct cases according to the amplitude of stress within the 6061-T6 Al target:

- $\sigma_{Al} < HEL_{Al}$: Hooke laws apply for both the aluminum target and silica fiber (elasticity).
- $HEL_{SiO2} > \sigma_{Al} > HEL_{Al}$: Hooke laws apply only for silica while aluminum behaves hydrodynamically.

The state of strain within the silica fiber is obtained from the set of Eq. (9a) and Eq. (9b) as follows:

$$\varepsilon'_z = \frac{\sigma'_z}{E_{SiO2}} - 2 \cdot \nu_{SiO2} \cdot \frac{\sigma'_r}{E_{SiO2}} \quad (42a)$$

$$\varepsilon'_r = \frac{\sigma'_r}{E_{SiO2}} \cdot (1 - \nu_{SiO2}) - \nu_{SiO2} \cdot \frac{\sigma'_z}{E_{SiO2}} \quad (42b)$$

where σ'_z ($= \sigma_{SiO2}$) and σ'_r are the stresses coupled to the Silica material, from the target. One must keep in mind that both ν_{SiO2} and E_{SiO2} are stress-dependent as well. Besides, the strain values are negative since the materials experience compression. For sake of simplicity however, only the absolute strain values (*i.e.* positive) are considered here.

Assuming that the stress transfer is the same in all directions of space (hydrodynamic approximation), the state of stress applied to the fiber is then:

$$\sigma'_z = K \cdot \sigma_z \quad (43a)$$

$$\sigma'_r = K \cdot \sigma_r \quad (43b)$$

where K is the coupling coefficient, considered as a constant with respect to pressure ($K = 0.78$).

a. Elastic domain of Aluminum ($\sigma_{Al} < HEL_{Al}$)

Eq. (10) holds in planar shock loading ($\varepsilon_r = 0$) of the Aluminum material:

$$\sigma_r = \frac{\nu_{Al}}{1 - \nu_{Al}} \cdot \sigma_z \quad (44a)$$

Eq. (44 a) transposes into coupled stresses to the Silica material:

$$\sigma'_r = \frac{\nu_{Al}}{1 - \nu_{Al}} \cdot \sigma'_z \quad (44b)$$

Replacing σ'_r into Eq. (42a) and Eq. (42b) yields, after some rearrangements:

$$\varepsilon'_z = \frac{\sigma'_z}{E_{SiO2}} \left[1 - \frac{2 \cdot \nu_{Al} \cdot \nu_{SiO2}}{1 - \nu_{Al}} \right] \quad (45a)$$

$$\varepsilon'_r = \frac{\sigma'_z}{E_{SiO2}} \cdot \frac{(v_{Al} - v_{SiO2})}{(1 - v_{Al})} \quad (45b)$$

These two components of strain are then injected into the Bragg constitutive Eq. (26) to get:

$$\frac{\Delta\lambda_B}{\lambda_B} = \frac{\sigma'_z}{E_{SiO2}} \cdot \left[\left(1 - \frac{2 \cdot v_{SiO2} \cdot v_{Al}}{1 - v_{Al}} \right) - \frac{n^2}{2} \cdot \left[\frac{(v_{Al} - v_{SiO2})}{(1 - v_{Al})} \cdot (p_{11} + p_{12}) + \left(1 - \frac{2 \cdot v_{SiO2} \cdot v_{Al}}{1 - v_{Al}} \right) \cdot p_{12} \right] \right]$$

which simplifies to:

$$\frac{\Delta\lambda_B}{\lambda_B} = \frac{\sigma'_z}{(1 - v_{Al}) \cdot E_{SiO2}} \cdot \left[1 - v_{Al} \cdot (1 + 2 \cdot v_{SiO2}) - \frac{n^2}{2} \cdot [p_{11} \cdot (v_{Al} - v_{SiO2}) + p_{12} \cdot (1 - v_{SiO2} \cdot (1 + 2 \cdot v_{Al}))] \right] \quad (46)$$

b. Hydrodynamic domain of Aluminum ($HEL_{SiO2} > \sigma_{Al} > HEL_{Al}$)

For an impact stress in excess of the HEL of Aluminum, the following relation holds:

$$\sigma_z - \sigma_r = Y \quad (47)$$

where Y is the yield strength of 6061-T6 Aluminum, stress-dependent parameter (SCG model, Eq. (19)).

Eq. (47) is the basis for hydrodynamics approximation (quasi-hydrostatic state-of-stress). Any shear stress in excess of the Y -value is dissipated into material flow and the impact stress σ_z is nearly equivalent to the pressure P (see Eq. (15a)).

This equation is transposed into coupled stresses to the Silica material by using Eq. (43a) and Eq. (43b):

$$\sigma'_z - \sigma'_r = K \cdot Y \quad (48)$$

Replacing σ'_r into Eq. (42a) and Eq. (42b) yields, after some rearrangements:

$$\varepsilon'_z = \frac{\sigma'_z}{E_{SiO2}} \cdot (1 - 2 \cdot v_{SiO2}) + \frac{2 \cdot K \cdot Y}{E_{SiO2}} \cdot v_{SiO2} \quad (49a)$$

$$\varepsilon'_r = \frac{\sigma'_z}{E_{SiO2}} \cdot (1 - 2 \cdot v_{SiO2}) - \frac{K \cdot Y}{E_{SiO2}} \cdot (1 - v_{SiO2}) \quad (49b)$$

These two components of stress are then injected into the Bragg constitutive equation Eq. (26).

After simplification, it yields:

$$\frac{\Delta\lambda_B}{\lambda_B} = \frac{\sigma'_z}{E_{SiO_2}} \cdot (1 - 2 \cdot \nu_{SiO_2}) \cdot \left[1 - \frac{n^2}{2} \cdot (p_{11} + 2 \cdot p_{12}) \right] + \frac{K \cdot Y}{E_{SiO_2}} \left\{ 2 \cdot \nu_{SiO_2} + \frac{n^2}{2} \cdot (p_{12} \cdot (1 - 3 \cdot \nu_{SiO_2}) + p_{11} \cdot (1 - \nu_{SiO_2})) \right\} \quad (50)$$

The first term of the equation is of hydrostatic origin (Eq. (18)). The second term is an added contribution that takes into account material flow.

For small pressure values, Eq. (50) evolves as:

$$\frac{\Delta\lambda_B}{\lambda_B} = \frac{\sigma'_z}{E_{SiO_2}} \cdot 0.267 + \frac{K \cdot Y}{E_{SiO_2}} \cdot 0.303 \quad (51)$$

The elasto-optic effect counterbalances the mechanical effect but the latter is still dominant (by +27 %).

It is interesting to notice that the Poisson coefficient of 6061-T6 Al greatly matters in the elastic domain of Aluminum (on account of elasticity) but does not play any role in the hydrodynamic domain. Eq. (50) also reveals the importance of the yield strength Y since both coefficients are of the same order of magnitude.

IV. EXPERIMENTAL

We first describe the experimental setup. Experimental Bragg spectra are then commented along with Bragg sensitivity under sustained shock pressure.

A. Description of the experiment

1. Optical set ups

The experimental setup is presented in Fig. 1 and shown in Fig. 7. Chirped Fiber Bragg Gratings (CFBGs) were photowritten in a ClearCurve™ singlemode fiber by IXBlue (Lannion, France). The central Bragg wavelength was 1605 nm and the peak reflectivity was approximately 40 %. CFBG were apodized and their effective length was 46 mm. The chirp rate of the CFBG was 0.08 nm/mm leading to a Full Width at Half-Maximum (FWHM) of 4 nm.

Chirping the grating provides two advantages: (i) the amount of reflected light is approximately 40 times greater than with a conventional grating (constant period) of similar length (*e.g.* FWHM ~ 0.1 nm for a 50-mm long grating), thus improving the SNR, and (ii) the monitoring of the signal reflected by the zero-stress Bragg peak (*i.e.* pristine grating part out of shockwave) enables to retrieve the shockwave velocity according to the principle of detonation velocity measurement, previously described.^{7,8,24}

In turn, the reference Bragg wavelength also depends on the position of the shockfront, this aspect has been incorporated into the spectral modeling as well.

Light from a broadband ASE source (Amplified Spontaneous Emission) is injected into the CFBG through a 3-port circulator and the light reflected by the CFBG is eventually analyzed by a spectrum analyzer. The ASE source (Amonics, ASL-CL-25-B-FA, 25 dBm) provides a broadband emission spectrum in the C + L band ([1525 nm – 1610 nm]).

Two spectrum analyzers have been used for this experiment of which transfer functions have been estimated by injecting the light from the ASE source and by recording the amplitude of each pixel, normalized with respect to the source spectrum.

a. Free-space Czerny-Turner (CT) spectrometer

The first spectrum analyzer is based on a free-space Czerny-Turner (CT) spectrometer (Horiba TRIAX 180) equipped with a 75-g/mm grating (Richardson, 53-756R). The dispersed light at the output is projected onto a 16-channel photodiode array (Hamamatsu G7151-16, BW = 300 MHz) of pixel size 80 μm (height) x 200 μm (width) and dark noise \sim 200 pA. The spectral resolution of the CT spectrometer was 6.2 nm/pixel. It was adjusted in a manner that the Bragg grating wavelength was coincident with pixel #3 (1605 nm). A strong crosstalk was observed between neighboring channels ($C_i = 28\%$) due to the quasi Gaussian nature of light distribution at focal point.

The photocurrents generated at each output were amplified and converted into voltages by transimpedance amplifiers built on a dedicated printed circuit board. Since the light output was more important on the zero-stress Bragg channel (pixel #1), we adjusted a lower transimpedance gain for this channel with respect to the others. Furthermore, the DC transmission at pixel #1 was essential for the adjustment of the optical setup so that the electronic bandpass for pixel #1 was DC-120 MHz while the bandpass of the other channels was 50 kHz – 120 MHz. The output voltages from the 16 channels were then connected to 50-Ohm inputs of two 8-channel digitizing oscilloscopes (LeCroy HDO8000).

b. Arrayed-Waveguide Grating (AWG) spectrometer

The second spectrum analyzer used is a 40-channel Arrayed-Waveguide Grating (AWG), custom-made by VLC Photonics on an integrated optics Silica chip and operating in the [1542 nm-1607 nm] range. The channel spacing was 1.7 nm (\sim 200 GHz). Each channel has a flat top transmission band with very sharp transition edges leading to negligible crosstalk between neighboring channels. Fibers are connected to the AWG chip using fiber arrays in order to carry the light to external photodetectors.

The expected Bragg shift was estimated for each flyer velocity and the corresponding AWG outputs were customarily connected to a series of 16 fast photoreceivers (FEMTO) in order to monitor the pressure profile of the shockwave.

Although CFBG specifications were initially designed for the CT spectrometer, the CFBG were used with both CT and AWG spectrometers. As a consequence, the signal from the pristine part of the Bragg grating was split over 3 pixels (1603.4 nm, 1605 nm, 1606.4 nm) instead of only one for the CT spectrometer. Each 3 AWG output was monitored with

another series of 3 medium-bandwidth (DC - 400 MHz) photoreceivers (FEMTO) in order to monitor the velocity profile of the shockwave. The other channels were connected to photoreceivers of higher bandwidth (10 kHz – 2 GHz).

The 16 amplified outputs were then sent to two 8-channel digitizing oscilloscopes (Le Croy HDO8000), triggered by an external signal provided by the ESP of the gas gun.

2. Gas gun set up

The flyer and target both have the same diameter of 90 mm. The thicknesses of the flyer and target are respectively 20 mm and 55 mm. According to hydrodynamics modelings (OURANOS hydrodynamic code), the pressure level is sustained over a distance of 30 mm before the shock pressure drops down because of lateral and back release waves. The grating then experiences a large stress gradient and is eventually broken. The setup dimensions are chosen in such a way that the whole length of the Bragg grating is actually under shock when release waves start to reach the grating.

The CFBG is positioned along the target axis (z-axis) and the short wavelength part is placed near the surface taken as a reference in position (*i.e.* $\lambda_B = 1603$ nm at $x = 0$ mm and $\lambda_B = 1607$ nm at $x = 46$ mm).

The fiber was not recoated after Bragg grating photowriting but sleeved within a Teflon (PTFE) tube or directly bonded to Aluminum using liquid glue (Araldite).



FIG 7. View of the experiment: left : CT-spectrometer, right : AWG spectrometer

The Aluminum flyer is launched by the gas gun over a transfer plate at different impact velocities. Each target is equipped with Manganin or Carbon gauges depending on impact stress level. Below 2 GPa, Carbon gauges were used while Manganin gauges were used above 1 GPa. The gauges were placed on a surface perpendicular to z-axis, at 5 mm from the impact surface. ESPs are also used for impact velocity and tilt measurements. The uncertainty in flyer velocity is about ± 2 mm.

B. Experimental results

1. Electronic signals (shots #1-6)

Several tests were performed at different impact stresses in the range [0 – 4 GPa], thus covering both the elastic and plastic domains of 6061-T6 aluminum. The experimental parameters of all shots are described in Tables II and III.

For each shot, Table II gives the experimental conditions while Table III gives parameters for impact test with gas gun launcher.

TABLE II. Experimental parameters associated to each shot

Shot #	Spectrometer type	Fiber coating (External Diameter ED)	Delay time (μ s) between impact and observed sustained shock	Reference Bragg wavelength (nm)	Number of fiber breaks during shock propagation
#1	CT	Teflon tube (700 μ m)	4.72	1604.17 \pm 0.01	3
#2	CT	Teflon tube (700 μ m)	4.87	1604.21 \pm 0.01	4
#3	CT	Epoxy bonding (400 μ m)	3.8	1603.94 \pm 0.01	none
#4	AWG	Epoxy bonding (400 μ m)	4	1603.99 \pm 0.01	none
#5	AWG	Epoxy bonding (400 μ m)	4	1603.99 \pm 0.01	none
#6	AWG	Epoxy bonding (400 μ m)	5.1	1604.26 \pm 0.01	none

TABLE III. Parameters for impact test with gas gun launcher

Shot #	Flyer velocity (m/s) (ESP)	Impact stress (GPa) (calculated, measured*)	Bragg wavelength (nm) [sustained shock]	Bragg shift (nm) [sustained shock]
#1	315.5 \pm 6.3	2.33 \pm 0.05	1582.7 \pm 0.5	-21.5 \pm 1
#2	515.1 \pm 10.3	3.90 \pm 0.08	1575.5 \pm 0.5	-28.7 \pm 1
#3	521.6 \pm 10.4	3.96 \pm 0.1	1578.8 \pm 0.5	-25.1 \pm 1
#4	521.2 \pm 10.4	3.95 \pm 0.1	1577.3 \pm 0.2	-26.7 \pm 0.5
#5	91.6 \pm 1.8	0.66 \pm 0.01	1597.8 \pm 0.2	-6.2 \pm 0.5
#6	205 \pm 4.1	1.49 \pm 0.03	1592 \pm 0.2	-12.3 \pm 0.5

A first series of 3 shots (#1-3) was performed with the CT spectrometer while a second series of 3 shots (#4-6) was performed with the AWG spectrometer. Furthermore, fibers were sleeved within Teflon tubes for shots #1-2 or directly bonded to aluminum using liquid epoxy for shots #3-6.

Fig. 8 to 10 and Fig. 11 to 13 show the raw electronic signals acquired by the oscilloscopes with the first series of shot (#1-3) and the second series of shots (#4-6) respectively. Raw signals are displayed on Fig. 8-to-13 are corrected for ASE source spectrum and arbitrary shifted for sake of clarity. The raw signals obtained with the free-space CT spectrometer show a strong interchannel crosstalk that manifests itself as an unconstant baseline (mostly on neighboring pixels to pixel #1).

Conversely, the raw signals obtained with the AWG spectrometer do not show any crosstalk. Signal saturation was observed on channel #7 between delay times 4 μ s and 7 μ s in Fig. 10 (shot #3), but this had no influence on the estimation of the Bragg shift that is calculated at a shorter time delay (3.8 μ s) after impact.

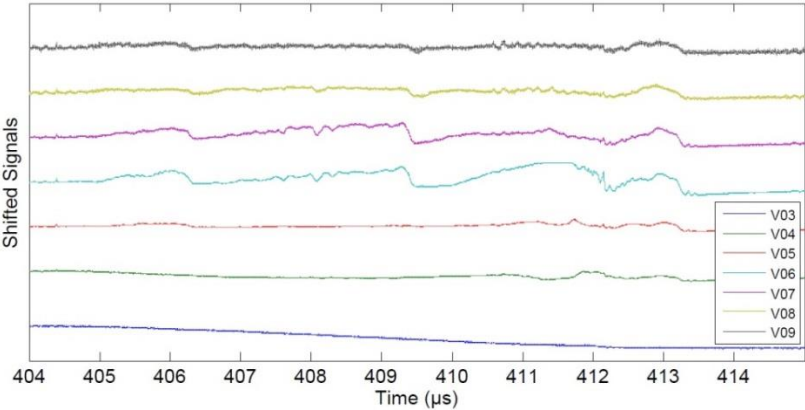


FIG. 8. Raw electronic signals for shot #1, 315.5 m/s, 2.33 GPa, CFBG in Teflon tubing (ED = 700 μ m), CT spectrometer

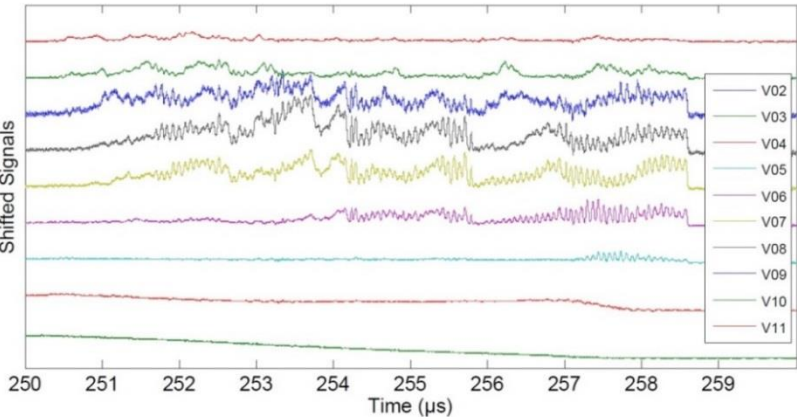


FIG. 9. Raw electronic signals for shot #2, 515.1 m/s, 3.9 GPa, CFBG in Teflon tubing (ED = 700 μ m), CT spectrometer

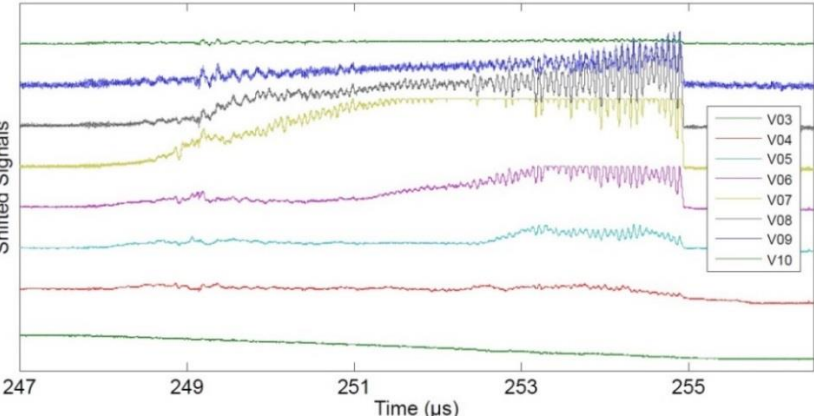


FIG. 10. Raw electronic signals for shot #3, 522 m/s, 3.96 GPa, CFBG directly bonded onto aluminum (ED = 400 μ m), CT spectrometer

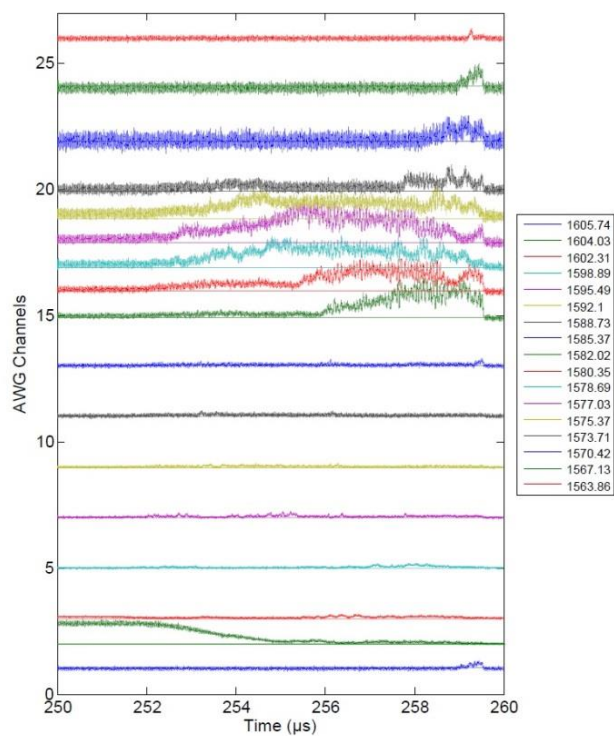


FIG. 11. Raw electronic signals for shot #4, 522 m/s, 3.95 GPa, CFBG bonded onto aluminum (ED = 400 μm), AWG spectrometer

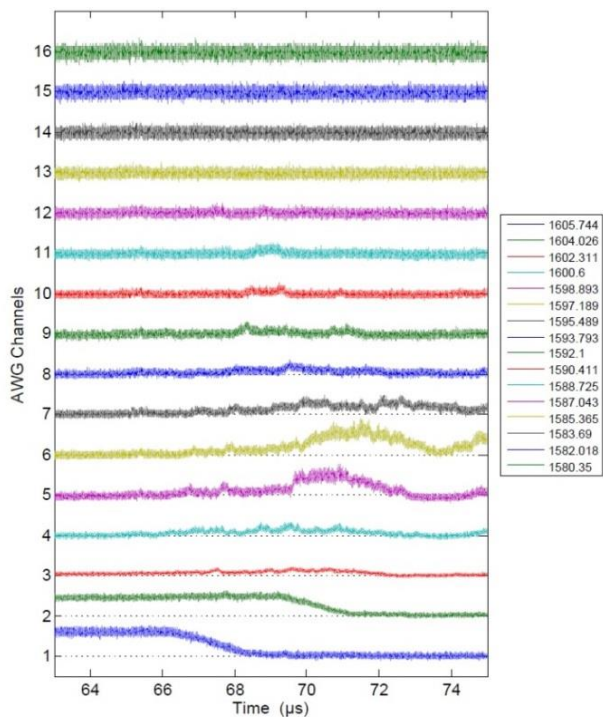


FIG. 12. Raw electronic signals for shot # 5, CFBG bonded onto aluminum (ED = 400 μm), 91 m/s, 0.66 GPa, AWG spectrometer

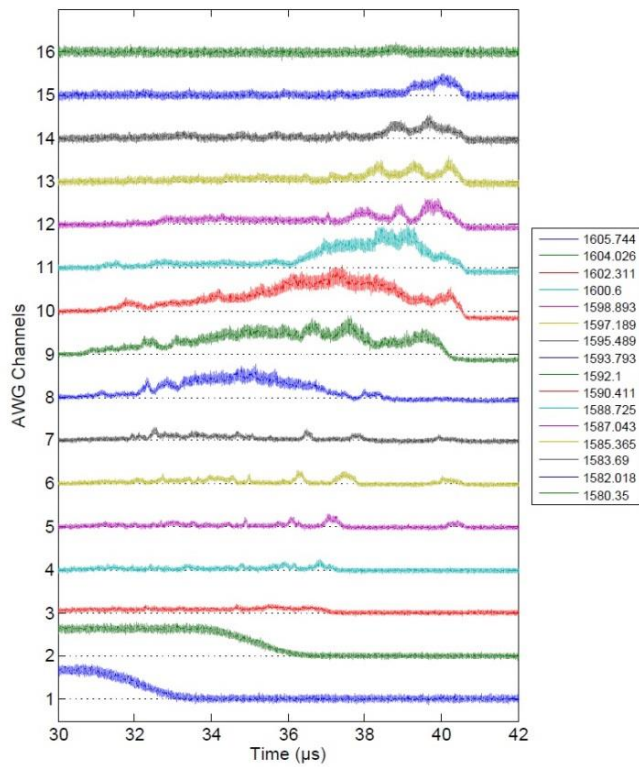


FIG. 13. Raw electronic signals for shot # 6, CFBG bonded onto aluminum ($ED = 400 \mu\text{m}$), 199 m/s, 1.49 GPa, AWG spectrometer

In the pressure range of interest, the fiber was not expected to break within the sustained shock. The number of fiber breaks is given in table II for each shot. The fiber actually broke several times on shots #1 and #2 on account of spalling generated by release waves at the target-fiber interface due to impedance mismatch and the possible presence of air bubbles within the adhesive layer. It is worthwhile to notice the absence of fiber break on shots #3 to # 6 because of a smaller integration diameter and a better fiber gluing with a cross-linking adhesive.

For each shot, a time of observation was chosen for the Bragg spectrum under sustained shock condition that gives the best accuracy on spectral measurements, mainly dependent on electronic noise.

As shown in Fig. 2, only a portion of the CFBG is actually under sustained shock, while another part is under the elastic precursor and the remaining part is pristine (out of shock). On fig. 8 to 10, the reflected signal of the pristine part of the grating is observed on pixel #1. The reflected signal attributed to the elastic precursor is observed on pixel #2. Finally, the reflected signals of the grating part under sustained shock are observed on all other remaining pixels.

2. Reconstruction of spectral data

As an example, Fig. 14 shows the signals obtained during shot #2 (with the free-space CT spectrometer), corrected for optical crosstalk and run-averaged over 10 sampling points in order to improve the SNR. Only the pixels #1 to #6 are shown for clarity in the spectral domain of interest for this shot. A crosstalk coefficient of 28 % was found optimal in order to retrieve a zero signal on all channels at both beginning and end of shot sequences. No crosstalk correction was necessary for shots #4-6 (with the AWG) which greatly simplified data analysis.

a. Pristine grating part

The signal reflected by the pristine grating part was observed on pixel #1. It provides the time evolution of the shockfront (Fig. 14). Since the elastic precursor travels faster ($C_L \sim 6400$ m/s) than the plastic shockwave ($C_p \sim 5700$ m/s), the shock velocity obtained from the signal reflected at the reference (zero-stress) Bragg wavelength is that of the elastic precursor.

b. Elastic precursor

As a support to this observation, one may calculate the shock velocity as obtained from the raw signal of pixel #1 in fig. 8 to 10. The time delay between impact and signal shutdown from pixel #1 is about $7.2 \mu\text{s} \pm 0.05 \mu\text{s}$. Since the effective length of the grating is $46 \text{ mm} \pm 0.5 \text{ mm}$, it yields a mean shock velocity of approximately $6390 \text{ m/s} \pm 110 \text{ m/s}$. According to Isbell *et al.*⁶², the elastic wave travels at a longitudinal speed of $6328 \text{ m/s} + 173 \text{ P (GPa)}$. Our estimation of elastic shock velocity is thus in accordance with the reported value ($\sim 6375 \text{ m/s}$ for $P = 0.4 \text{ GPa}$ (HEL of 6061-T6 Al)) thus demonstrating the pertinence of this measurement. However, the uncertainty in velocity is relatively large because the SNR displayed in Fig. 14 is still poor (~ 40) in spite of the run-averaged procedure.

The spectral contribution of the elastic precursor is observed on pixel #2. We expect from calculated Bragg spectra (based upon OURANOS code) a ratio of spectral intensity precursor/initial grating of $8.5 \% \pm 0.3 \%$ while the experimental ratio at the end of the shock ($10 \mu\text{s}$) was $7.7 \% \pm 0.2 \%$.

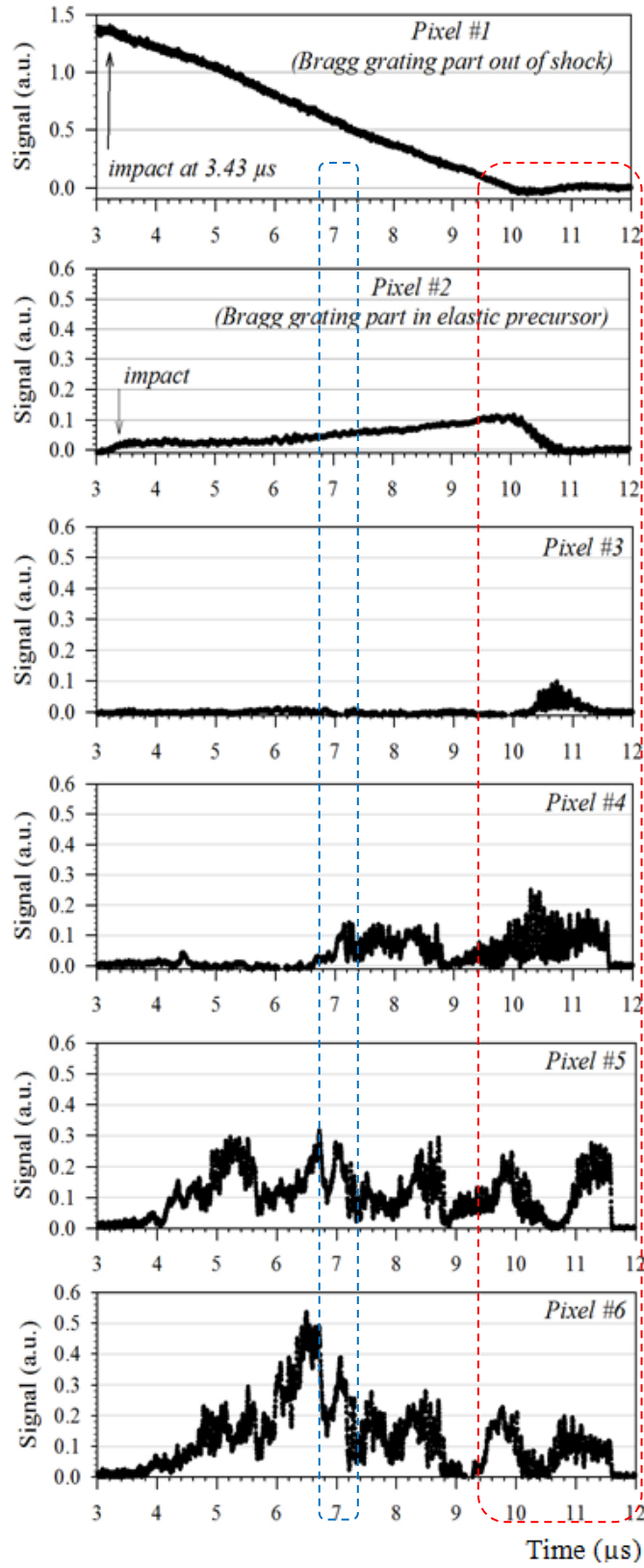


FIG. 14. Electronic signals corrected for crosstalk influence ($C_i = 28\%$) for shot #2 (515 m/s). Only pixels #1 to #6 are shown. The first zone (around 7 μs) depicts the Bragg spectrum under sustained shock. The last part (10-12 μs) corresponds to interaction by release waves.

c. Steady-state shock plateau

The Fig. 15 depicts how the reference Bragg wavelength λ_{B0} is estimated for the grating part under sustained shock condition, according to OURANOS numerical simulations (Fig. 2). The estimations of Bragg wavelength shifts were performed on best resolved shock plateau. Since some fiber break occurred, the delay times of observations are not the same for all shots.

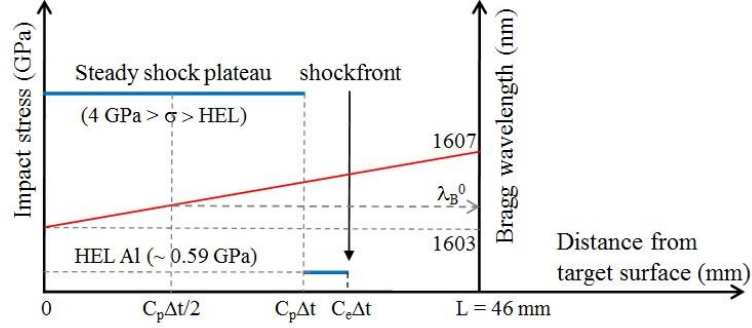


FIG. 15. Sketch of the 3 grating parts involved in each shot (part within sustained shock plateau, part within elastic precursor, pristine part) and evolution of Bragg wavelength with distance from target surface within the CFBG.

The delay time between impact and time of observation was then estimated and given in table II.

We considered the position at middle of the sustained shock plateau given by $x = C_p \cdot \Delta t / 2$ where Δt is the time delay between impact and sustained shock observation and C_p is the plastic shock velocity (5700 m/s).

The reference Bragg wavelength for the grating part under steady shock is then:

$$\lambda_B^0 = 1603 + 4 \cdot \frac{x}{L} = 1603 + 2 \cdot \frac{C_p \cdot \Delta t}{L} \approx 1603 + 0.248 \cdot \Delta t \quad (52)$$

The uncertainty in reference Bragg wavelength was 0.01 nm. Actually, the uncertainty in Bragg shift is dominated by the uncertainty in the Bragg wavelength under shock.

From the raw data displayed on Fig. 8 to 13, the Bragg spectra on sustained shock were reconstructed from each signals and displayed for each shot. Fig. 16 and 17 show the Bragg spectra under sustained shock for the first series of shots #1 to #3 (CT-spectrometer) and the second series of shots #4 to #6 (AWG spectrometer) respectively. The mean reference Bragg wavelength of 1605 nm is also indicated as a guide to the eye and illustrates the wavelength shift for each shot.

The Bragg wavelengths of the grating portion under sustained shock have been determined by Gaussian fittings, motivated by the fact that the Bragg spectrum is partly broadened by the chirp factor of the CFBG along the sustained shock and by the transfer function of the spectrometer. A satisfactory fit is provided with shots #4 - #6 on account on the smaller channel

spacing (1.7 nm) and absence of crosstalk of the AWG spectrometer, yielding an uncertainty in Bragg wavelength of ± 0.2 nm. However, the Gaussian fit is less conclusive for shots #1 - #3 because the CT spectrometer shows a strong optical crosstalk ($C_i = 28\%$) and its channel spacing is larger than that of the AWG. The uncertainty in Bragg wavelength measurement is thus larger (± 0.5 nm) than with the AWG spectrometer. The mean wavelengths of Gaussian fittings are listed in table III along with respective shot conditions (flyer velocity, impact strength). For each flyer velocity (measured by ESP), the impact stress (in GPa) was calculated using Eq. (8).

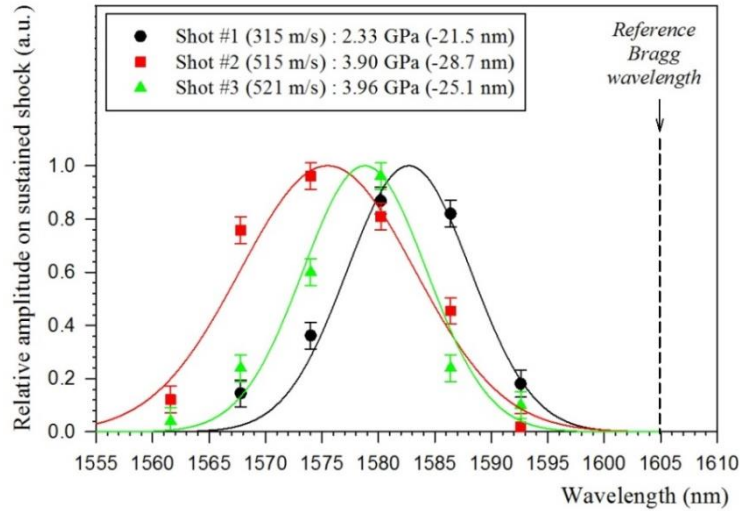


Fig. 16. Bragg spectra on sustained shock reconstructed from signal data for shots #1 to #3 (CT-spectrometer). Delay times between impact and observation are given in Table II.

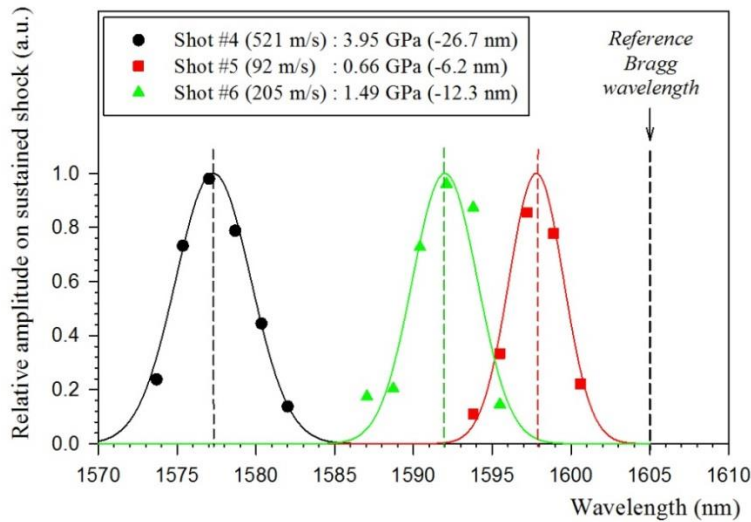


Fig. 17. Bragg spectra on steady shock reconstructed from signal data for shots #4 to #6 (AWG-spectrometer). Delay times between impact and observation are given in Table II.

3. Bragg grating sensitivity vs impact stress

The Bragg wavelength shifts measured on sustained shock plateau were then plotted with respect to calculated impact stresses as shown in Fig. 18.

Experimental data are compared to the theoretical evolution for the Bragg shift as given by Eq. (46) and Eq. (50) respectively for the elastic and hydrodynamic domains of Aluminum. The agreement between experimental data and theoretical predictions is satisfactory, therefore providing a confirmation of all previous hypotheses. The deviation between theory and experimental data obtained with the AWG is less than $\pm 2\%$. The uncertainty of experimental data obtained with the CT spectrometer is larger but the Bragg shifts are actually consistent with theory.

The Bragg sensitivity, as given by the first derivative of the Bragg wavelength shift with respect to stress, is plotted as well (in dotted lines) for both domains. One can see that it exhibits a sharp discontinuity that is due to the arbitrary separation between the two mechanical domains of Aluminum. In practice, the curve of sensitivity vs stress is supposed to behave continuously, calling for a more complex model (hybrid model partly elastic and hydrodynamic) than the current one.

In the elastic domain of Aluminum, the wavelength-to-stress sensitivity of the CFBG is quite high (between -9 nm/GPa and -12 nm/GPa) on account of the orientation of the stress ellipsoid, towards the direction of shock, along the fiber axis.

In the hydrodynamic domain however, the Bragg sensitivity is lower (~ -7 to -9 nm/GPa) and tends to decrease with increasing impact stress until reaching a null value at ~ 3.6 GPa. It is interesting to compare this value to the usual hydrostatic sensitivity of Bragg grating which is around -3.5 pm/MPa, *i.e.* half the value reported here.

The Bragg sensitivity of the CFBG embedded within Aluminum targets is therefore strongly nonlinear with impact stress.

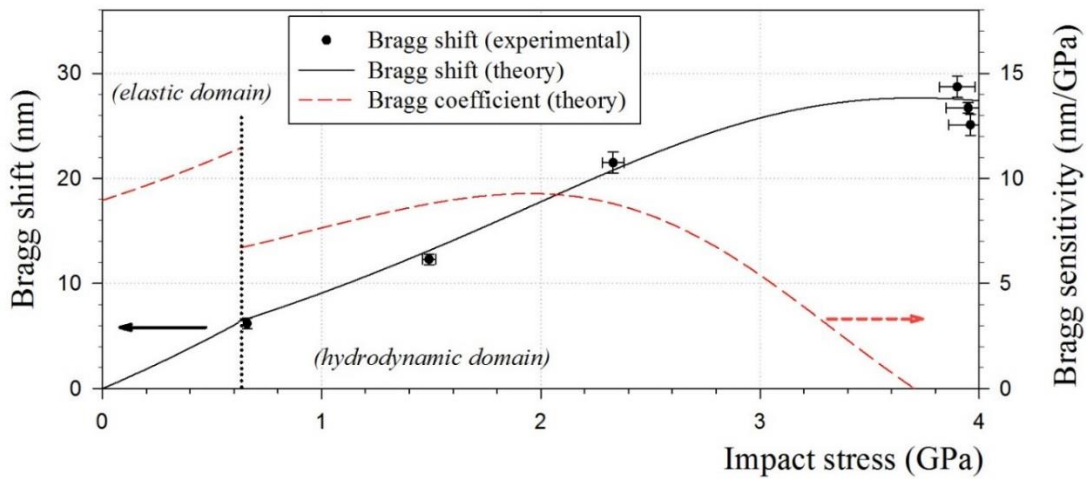


FIG. 18. Evolution of the Bragg shift of the CFBG with respect to impact stress, in the range [0 – 4 GPa]. The line drawing corresponds to the theoretical Bragg shift as calculated using Eq. (46) and Eq. (50) for the elastic and hydrodynamic domains of 6061-T6 Aluminum respectively. The dotted line shows the Bragg sensitivity in the same pressure range. The pressure coupling coefficient from Aluminum to Silica is taken as constant ($K = 0.78$).

V. DISCUSSION

This study highlights the nonlinear behavior of the Bragg shift *vs* planar shock stress in the experimental configuration involving Aluminum-based target and flyer. Aluminum (Al 6061-T6) was chosen because it is widely used in shock physics. Furthermore, the shock impedance of Aluminum in the hydrodynamic domain is close to that of Silica (still solicited in the elastic domain). The stress dependence of the yield strength (Y-value) of 6061-T6 aluminum according to the Steinberg-Cochran-Guinan (SCG) model³⁶ was incorporated in our model. Depending on impact stress, 6061-T6 Aluminum behaves either elastically (shear stress $\tau < Y/2$) or plastically ($\tau > Y/2$), leading to different stress ellipsoids within the target material.

Starting from the Bragg constitutive equations, linear photoelasticity is assumed in the stress range of interest. Since the p_{11} and p_{12} ‘Pockels’ photo-elasticity coefficients of Silica fiber are composition- and wavelength-dependent, we have taken into account new data recently obtained at 1550 nm for a pure Silica-core fiber, of close composition to the fiber used in our experiment (Corning Clearcurve™). The most important parameters of the model are the yield strength Y of the target material and the photoelastic coefficients of Silica. Surprisingly enough, the other mechanical parameters (E_{Si} , ν_{Si} , ν_{Al}) are less relevant. Furthermore, the evolution of refractive index (RI) with stress depends on the stress ellipsoid, itself dependent on whether the fiber is submitted to hydrostatic or planar impact loading. Setchell²⁹ and Dandekar *et al.*⁵¹ reported values of index-to-shock stress coefficients obtained under planar shock loading that differ by approximately a factor of 2 with respect to index-to-pressure coefficients reported by Vedam⁵⁸ and Zha *et al.*⁵³ under hydrostatic loading. Similarly, Barker and Hollenbach⁵⁶ provided a relationship for the Young modulus of silica *vs* stress applied in planar shock loading and Kondo⁵⁷ investigated the evolution of the Young modulus of silica under hydrostatic loading. In our case, despite the planar loading conditions, the target material behaves hydrodynamically for stress levels higher than the HEL value for 6061-T6 Al, *i.e.* 0.6 GPa. Consequently, the hydrostatic relationships provided by Zha *et al.*⁵³ and Kondo *et al.*⁵⁷ have been considered as most pertinent and used for the proposed model. Similarly, the model also uses the relationship provided by Zha *et al.*⁵³ that rules the evolution of the Poisson coefficient of silica with respect to hydrostatic pressure. In the elastic domain of Aluminum, the Poisson coefficient was considered as constant and equal to 0.34. It should be noticed that neither the Young modulus nor the Poisson coefficient of Aluminum (target material) does play any role in the hydrodynamic domain.

As the CFBG is solicited exclusively in its elastic domain in the range [0 – 4 GPa], the nonlinearity arises from constitutive parameters, mainly refractive index, Poisson coefficient and Young modulus of Silica. Another nonlinear contribution of lesser importance is strain hardening of 6061-T6 Al (*i.e.* increase of the yield strength Y with applied stress).

Finally, the last parameter of utmost importance is the pressure coupling coefficient (from the Aluminum target to the Silica fiber) that is estimated by 2D FEM modelings (OURANOS hydrodynamic code). Two calculations have been carried

out with respect to flyer speed (impact stress) with the aim to estimate the amount of pressure coupled from Aluminum to Silica. A first calculation (unrealistic) has been carried out without epoxy and a second one (realistic) was performed with the epoxy layer placed in-between Aluminum and Silica in order to analyze its influence on the pressure transfer from aluminum to silica. Without epoxy, the coupling coefficient increases at higher pressures witnessing an improved shock impedance matching in the intermediate pressure range (up to 4 GPa). With epoxy, the coupling coefficient remains roughly constant within calculation uncertainties, at the value $K = 0,78 \pm 0.05$, similar to the analytical value calculated at low pressure (less than 0.4 GPa). Since a polymer sleeve is necessary both for practical handling and elimination of air bubbles, the model takes into account a constant value for the coupling coefficient, taken as 0.78.

For both domains (elastic, hydrodynamic), relationships are given for the Bragg shift as a function of impact stress that are in continuity at the HEL critical value (0.6 GPa) separating both domains. Differentiating those relationships provides the Bragg sensitivities *vs* impact stress. As a consequence of the sudden change in stress ellipsoid at this critical value, a discontinuity in sensitivity occurs that has no physical ground and calls for a more complex model that includes a smooth transition between elastic and hydrodynamic behaviors.

Let us suppose that all constitutive parameters are well-known and that the coupling coefficient is accurately defined by hydrodynamic code calculations, the objective is - from the point of view of the engineer - to retrieve the stress distribution along the target axis from the experimental Bragg spectra. However, this inverse calculation is an ill-posed problem since it requires the phase information along the CFBG length that is missing in spectrometric acquisitions. The method actually consists in calculating Bragg spectra (with Beam Propagation or Transfer Matrix methods that fall out the scope of this publication) from the stress distributions within the CFBG determined by the hydrodynamic code with elastic-plastic constitutive laws. Calculated Bragg spectra are then compared to the experimental ones. A least-square analysis between calculated and experimental spectra may enable to converge towards the most-likely stress distribution under any conditions.

In some configurations such as hydrostatic or planar shock loading investigated here, the corresponding stress distributions and velocities is modeled. In the case of a planar shock loading over 6061-T6 Aluminum plates, a simple model for the stress distribution at early times of shock propagation is described in fig. 15. It consists in two square functions of unknown pressure amplitudes traveling at different velocities (plastic shockwave C_p and elastic precursor C_L). In this very simplified configuration, the application of the experimental Bragg shift-to-stress Eq. (46) and Eq. (50) is useful.

Let us consider the use of weakly-reflective gratings, the square root of the reflectivity is related to the Fourier Transform of the index modulation, as given by⁶³:

$$\rho(\delta) = -j \cdot \int_{-L/2}^{L/2} C(z) \cdot \exp[-j \cdot (2 \cdot \delta \cdot z - \phi)] \cdot dz \quad (53)$$

Where Φ is the phase that is constant in unchirped grating, and δ is the detuning parameter given by:

$$\delta = \frac{2 \cdot \pi \cdot n}{\lambda} - \frac{\pi}{\Lambda} = 2 \cdot \pi \cdot n \cdot \left(\frac{1}{\lambda} - \frac{1}{\lambda_B} \right) \approx 2 \cdot \pi \cdot n \cdot \frac{\lambda - \lambda_B}{\lambda_B^2} \quad (54)$$

$C(z)$ is the Bragg coupling coefficient, given by :

$$C(z) = \frac{\pi}{\lambda} \cdot \Delta n(z) \cdot \eta \quad (55)$$

Where Δn is the index modulation (related to apodisation for instance) and η is the fraction of power guided within the photosensitive core (close to 0.8 for most singlemode fibers). The index modulation is considered as constant in the useful part of grating, so that $\Delta n(z) = \Delta n$.

During the shock, Δn does not change and so does the C -parameter that can be removed from the integral. Only the detuning and phase parameters actually change under shock.

In the absence of chirp, the Eq. (53) is solved according to the well-known relation for Bragg reflectivity:

$$\rho(\delta) = C \cdot L \cdot \text{sinc}(\delta \cdot L) \quad (56)$$

According to Fig. 15, the reflectivities of the Bragg peak associated to the plastic shock and elastic precursor may be written respectively:

$$R(\lambda_p) = |\rho \cdot \rho^*(\lambda_p)| = (C \cdot C_p \cdot \Delta t)^2 \cdot \text{sinc} \left(\frac{2 \cdot \pi \cdot n_p \cdot \Delta \lambda_p \cdot C_p \cdot \Delta t}{\lambda_B^2} \right)^2 \quad (57)$$

$$R(\lambda_e) = |\rho \cdot \rho^*(\lambda_e)| = (C \cdot (C_L - C_p) \cdot \Delta t)^2 \cdot \text{sinc} \left(\frac{2 \cdot \pi \cdot n_e \cdot \Delta \lambda_e \cdot (C_L - C_p) \cdot \Delta t}{\lambda_B^2} \right)^2 \quad (58)$$

where Δt is the delay time after impact and n_p and n_e are respectively the index of refraction for the fiber part within the plastic shock and elastic precursor respectively, deduced from the Bragg shifts $\Delta \lambda_p$ and $\Delta \lambda_e$.

The reflectivities (Eq. (57) and Eq. (58)) provide information about the length of the grating under shock while the Bragg shift (Eq. (46) and Eq. (50)) gives an estimation of the applied stress.

Experimentally, the CFBG may experience one or more breaks during shock propagation, probably due to spalling due to impedance matching at the interface (presence of air bubbles). It is important to notice that fiber breaks have no influence on Bragg shift measurement, but must be taken into account for the measurement of active Bragg lengths (in practice, the reflectivity drops down suddenly). Experimentally, we also noticed that Teflon tubing was quite deleterious in this aspect and that epoxy bonding was the most appropriate fiber conditioning.

VI. CONCLUSION

Fiber Bragg Gratings (FBGs) are gaining acceptance as velocity or pressure gauges in the field of detonation and shock physics on account of their high sensitivity, passive nature, small size, flexibility and electromagnetic immunity. High-bandwidth signal acquisition is required (digitizing oscilloscopes) and the SNR mainly depends on the acquisition electronics. FBGs provide direct temperature and strain sensing, the latter parameter being converted into stress with the help of a mechanical stress-to-strain model. The wavelength-encoded capability enables multiplexing (WDM) and provides reliable measurements even in harsh conditions. Additional benefits of FBGs in the domain of shock physics are the low shock-induced self-heating and the high Hugoniot Elastic Limit (HEL) of silica (8.8 GPa). For intermediate range of impact stress (*i.e.* less than the HEL value but albeit higher than conventional mechanical stress levels (several 100 MPa)), the practical consequences are a high strain sensitivity and the absence of temperature compensation of the Bragg signal.

While regular FBGs are usually considered as point sensors up to several-mm long, chirped FBGs (CFBGs) are investigated to provide wavelength-to-position discrimination with the purpose of monitoring pressure and velocity profiles over distance ranges of typically 100 mm. The practical use of CFBGs for monitoring detonation velocity of High Explosives (HEs) has been investigated by several research teams⁶⁻¹⁰ and is now well established. The crucial advantage of CFBGs in comparison with conventional FBGs is the distributed measurement capability that simplifies both sensor deployment, data retrieval and increases the number of data points which in turn improves the metrological resolution. CFBGs have found a useful application in the determination of Shock-to-Detonation Transition (SDT).

In this paper, the use of CFBGs as *in situ* pressure/velocity gauges is investigated theoretically and experimentally under inert planar shock loading conditions with a gas gun launcher and Aluminum flyer and target. Earlier shock monitoring experiments were investigated with several mm-long FBGs¹¹⁻¹⁵ and CFBGs have been investigated only recently for this purpose.¹⁷⁻¹⁸ The principle is the same as for velocity measurement except that the CFBG is not broken immediately by the shockwave, but few microseconds later by the release wave. Hence, as the shockwave travels through the grating, the length of the pristine part (out of the shock) decreases at the shockfront speed while the grating part within the shock is under compression. Therefore, the Full Width at Half-Maximum (FWHM) of the spectrum of the pristine part shrinks progressively as the shockwave comes forward. The amount of light reflected back thus provides a measurement of the shockwave position as a function of time, from which the shockwave velocity may be estimated by linear regression, in a similar manner as previous experiments with HEs. Within metallic materials as targets (*e.g.* aluminum), the shockfront is associated with an elastic precursor that travels faster than the plastic shockwave. The Bragg spectrum of the compressed part is shifted to lower wavelengths (*i.e.* blue-shifted), the Bragg shift being stress-dependent. The amplitude of Bragg reflection spectrum provides

a complementary information related to the length of the grating part under sustained stress. At first glance, the reflectivity is proportional to the square of the grating length for weakly-reflecting FBGs. In the intermediate range of shock stress (*i.e.* less than the HEL of silica), CFBGs thus provide a simultaneous measurement of both shockwave velocity and state-of-stress within the target material. However, the estimation of the state-of-stress is less straightforward than the velocity as the wavelength-to-stress relation linking the Bragg wavelength shift to the shock stress requires both stress-to-strain and wavelength-to-strain relationships. A complete model requires to (i) know the state of stress within the target material, (ii) calculate the stress coupling coefficient due to imperfect impedance matching between the target material and the silica fiber, (iii) convert the state-of-stress into a state-of-strain within the silica fiber taking into account Hooke's laws and finally, (iv) translate the strain data into observable Bragg wavelength shifts (taking into account photo-elasticity and density change). Moreover, many constitutive parameters of silica (Young modulus, Poisson coefficient, refractive index) and of usual metals (yield strength Y) are stress-dependent which brings additional complexity.

In this work, a theoretical analysis of the Bragg wavelength-to-stress sensitivity is provided in the intermediate stress range [0 – 4 GPa], below the Hugoniot Elastic Limit (HEL) of silica. Starting from the linear Bragg constitutive equations, the state-of-stress within the target material (Aluminum 6061-T6) is firstly determined for both elastic (shear stress $\tau < Y/2$) and hydrodynamic domain (shear stress $\tau > Y/2$), taking into account the SCG model. Then, the state-of-stress within the silica fiber is estimated taking into account a constant coupling coefficient ($K = 0.78$), determined by analytical estimation (for impact stress less than 0.6 GPa) and by hydrodynamic code FEM modelings (OURANOS). The state-of-strain in the Silica fiber is then calculated considering that silica behaves elastically in this pressure range of interest ([0 – 4 GPa]), from which both the evolution of Bragg shift and sensitivities are determined with respect to impact stress for both domains. In the elastic domain of Aluminum, the wavelength-to-stress sensitivity of the CFBG is quite high (between -9 nm/GPa and -12 nm/GPa according to impact stress) on account of the orientation of the stress ellipsoid, towards the direction of shock, along the fiber axis. In the hydrodynamic domain however, the Bragg sensitivity is much lower (~ -7 to -8 nm/GPa according to impact stress) and tends to decrease with increasing impact stress until reaching a null value at ~ 3.6 GPa. The Bragg sensitivity of the CFBG embedded within Aluminum targets is therefore strongly nonlinear with impact stress.

In order to compare with the theoretical approach, an experimental calibration of CFBG under planar shock loading configuration has been performed. 6061-T6 Aluminum flyers have been launched at several velocities by a gas gun over transfer plates (targets) of similar material. CFBGs (zero-stress wavelength = 1605 nm, FWHM = 4 nm) were located within the target and bonded along the axis with glue.

Two spectrum analyzers were used for the experiments, the first one used a free-space Czerny-Turner (CT) spectrometer (channel spacing ~ 6.2 nm) and the second one used an Arrayed-Waveguide Grating (AWG) spectrometer designed in integrated optics (channel spacing ~ 1.7 nm). The optical setup also involves a broadband light source (ASE), transimpedance amplifiers and digitizing oscilloscopes. The AWG-based spectrometer provided the most accurate results on account of smaller channel spacing and also unnoticeable interchannel crosstalk.

With the aim to calibrate the wavelength-to-stress response of CFBGs, both the elastic precursor and the sustained part of the plastic shock were analyzed with respective periods of time of $0.6 \mu\text{s}$ and $5 \mu\text{s}$ post-impact. The shock velocity that is measured by progressive extinction of the Bragg signal reflected back by the pristine CFBG is that of the elastic precursor and agrees well with expected value. For each portion of sustained plastic shockwave, the Bragg spectra were reconstructed from signal data and Gaussian-fitted with satisfactory goodness-of-fit. The experimental Bragg wavelength shifts were then plotted with respect to impact stress along with theoretical models for both elastic and hydrodynamic domains of 6061-T6 Al.

Experimental data agree well with theoretical predictions in the intermediate range of stress [0 – 4 GPa] investigated here, therefore validating the model for planar shock loading of aluminum flyer/target. The deviation between theoretical calculation and experimental data recorded with the AWG is less than $\pm 2\%$. This work opens large perspectives for the future of shock physics either for inert materials or for HEs.

First of all, our investigations were restricted to the intermediate stress range [0 – 4 GPa] for which data were available about pressure dependence of constitutive parameters, especially the evolution of the Young modulus of Silica under hydrostatic loading. Extended data on broader range are therefore needed in order to extend the stress range of interest.

Secondly, silica may withstand compressive stress up to 16 GPa and therefore, CFBG are likely to be used up to this stress value despite the occurrence of a phase transition (permanent densification) undergone by silica above its HEL value. To our knowledge, no such experiment has been reported yet. An important question arises whether linear photo-elasticity is still a valid assumption up to this stress value or if nonlinear photoelasticity must be considered instead.

Thirdly, this study highlights the nonlinear behavior of the Bragg shift *vs* applied stress. Since the CFBG remains in its elastic domain, the nonlinearity arises from constitutive parameters, mainly refractive index, Poisson coefficient and Young modulus of Silica. Another nonlinear contribution of lesser importance is strain hardening of 6061-T6 Aluminum (*i.e.* increase of the yield strength with applied stress).

Fourthly, an inverse calculation of the stress distribution from Bragg spectra is an ill-posed problem as phase information is missing from spectrometric acquisitions. Nevertheless, stress distributions and velocities may be modeled *a priori* in simplified configurations (*e.g.* hydrostatic or planar shock loading) and stress data may be retrieved with the help of the experimental wavelength-to-stress relations provided in this work.

Finally, the results of this paper may be further extended to other configurations such as hydrostatic shock loading and detonation. The extension to pure planar shock loading requires the use of relationships from Barker and Hollenbach⁵⁶ (Eq. 38) and Setchell²⁹ (Eq. 34) for the Young modulus and RI change respectively in lieu of the relationships provided by Kondo *et al.*⁵⁷ (Eq. 40)) and Zha *et al.*⁵³ (Eq. 35) that are valid for hydrostatic loading. We are also looking forward to using this model with HEs showing elasto-plastic behavior and high-HEL materials such as sapphire or fused silica. A significant increase in Bragg sensitivity (for a CFBG aligned along the direction of shock) is expected due to a more favorable stress ellipsoid by comparison to the hydrodynamic configuration. The choice of fused Silica as target material should also improve the stress coupling to the silica fiber on account of ideal impedance matching. In all case, fiber bonding is necessary for both practical handling and elimination of air bubbles but it requires accurate FEM modelings to be performed in order to estimate the pressure coupling coefficient that reveals itself as an important parameter of the model.

ACKNOWLEDGMENTS

This work has been performed within the ANDROMEDE Project, funded by the DGA (*Direction Générale de l'Armement*), in the framework of the ASTRID Program of the ANR (*Agence Nationale de la Recherche*).

The authors would like to thank C. Collet and L. Blarasin (ArianeGroup, Vert-le-Petit, France) for their contribution to the ANDROMEDE Project.

REFERENCES

- ¹D.R. Goosman, J. Wade, R. Garza, G. Avara, T. Crabtree, A. Rivera, D. Hare, D. Tolar and B. Bratton, 26th Int. Congress On High Speed Photography and Photonics, Alexandria (USA), September 19-24, 2004, Proc. SPIE **5580**, 517 (2004).
- ²Z. Rosenberg, D. Yaziv and Y. Partom, J. App. Phys. **51**, 3702 (1980).
- ³H. Vantine, J. Chan, L. Erickson, J. Janzen, R. Weingart and R. Lee, Rev. Sci. Instr. **51**, 116 (1980).
- ⁴L.M. Barker, R.E. Hollenbach, J. Appl. Phys. **43**, 4669 (1972).
- ⁵R.L. Gustavssen, S.A. Sheffield and R.R. Alcon, J. Appl. Phys. **99**, 114907 (2006).
- ⁶J. Benterou, C.V. Bennett, G. Cole, D.E. Hare, C. May and E. Udd, SPIE Defense, Security and Sensing (DSS), Orlando FL, USA, Proc. SPIE **7316** (2009).
- ⁷S. Magne, A. Lefrançois, J. Luc, G. Laffont and P. Ferdinand, 5th European Workshop on Optical Fiber Sensors (EWOFS), Krakow (Poland), Proc. SPIE **8794**, 87942K (2013).
- ⁸G. Rodriguez, R.L. Sandberg, Q. McCulloch, S.I. Jackson, S.W. Vincent and E. Udd, Rev. Sci. Instrum. **84**, 015003 (2013).
- ⁹S. Gilbertson, S.I. Jackson, S.W. Vincent and G. Rodriguez, Appl. Opt. **54** (13), 3849 (2015).
- ¹⁰P. Wei, H. Lang, T. Liu and D. Xia, Sensors **17**, 2552 (2017)
- ¹¹P.G. Van't Hof, L.K. Cheng, J.H.G. Scholtes and W.C. Prinse, 27th Int. Congress on High-speed photography and Photonics, Proc. SPIE **6279**, 62791Y (2007).
- ¹²X. Deng, G. Chen, Q. Peng, Z. Li, J. Meng and J. Liu, Rev. Sci. Instrum. **82**, 103109 (2011).
- ¹³G. Rodriguez, R.L. Sandberg, B.M. Lalone, B.R. Marshall, M. Grover, G. Stevens and E. Udd, Proc. SPIE **9098**, Fiber Optic Sensors and Applications XI, 90980C (2014).
- ¹⁴R.A. Sandberg, G. Rodriguez, L.L. Gibson, D.M. Dattelbaum, G.D. Stevens, M. Grover, B.M. Lalone and E. Udd, 18th APS-SCCM and 24th AIR APT, J. Phys. Conf. Series **500**, 142031 (2014).
- ¹⁵E. Shafir, S. Zilberman, A. Ravid, B. Glam, G. Appelbaum, A. Fedotov Gefen, Y. Saadi, N. Shafir, G. Berkovic, 23rd International Conference on Optical Fiber Sensors (OFS 23), Santander (Spain), Proc. SPIE **9157**, 915713 (2014).
- ¹⁶G. Rodriguez, M. Jaime, F. Balakirev, C.H. Mielke, A. Azad, B.M. La Lone, B. Henson and L. Smilowitz, Opt. Exp. **23** (11), 14219 (2015).

- ¹⁷Y. Barbarin, A. Lefrançois, S. Magne, K. Woirin, F. Sinatti, A. Osmont and J. Luc, Proc. SPIE **9960** (Interferometry XVIII), San Diego (CA), 99600U (2016).
- ¹⁸G. Rodriguez and S.M. Gilbertson, Sensors **17**, 248 (2017).
- ¹⁹T. Erdogan, J. Lightwave Technol. **15** (8), 1277 (1997).
- ²⁰A.D. Kersey, M.A. Davis, H.J. Patrick, M. Leblanc, K.P. Koo, S.G. Askins, M.A. Putnam and E.J. Friebele, J. Lightwave Technol. **15** (8), 1442 (1997).
- ²¹H. Sugiura, K. Kondo and A. Sawaoka, J. Appl. Phys. **52**, 3375 (1981).
- ²²F. Malaise, J-M. Chevalier, I. Bertron and F. Malka, J. Phys. IV **134**, 929 (2006).
- ²³J. Wackerle, J. Appl. Phys., **33** (3), 922 (1962).
- ²⁴Y. Barbarin, A. Lefrançois, G. Zaniolo, V. Chuzeville, L. Jacquet, S. Magne, J. Luc and A. Osmont, Proc. SPIE **9480**, 9480-25 (2015).
- ²⁵A. Ravid, E. Shafir, S. Zilberman, G. Gerkovic, B. Glam, G. Appelbaum and A. Fedotov Gefen, 18th APS-SCCM and 24th AIR APT, J. Phys. Conf. Series **500**, 142029 (2014).
- ²⁶L. Bouyeron, A. Lefrançois, J. Luc, H-C. Seat, 13^{ème} Colloque International Francophone sur les Méthodes et Techniques Optiques pour l'Industrie (CMOI), Orléans, France (2013) (in french).
- ²⁷LASL Shock Hugoniot data, Los Alamos Series on dynamic material properties, S. P. Marsh editor, University of California Press, (1980).
- ²⁸M.G. Xu, L. Reekie, Y.T. Chow and J.P. Dakin, Electron. Lett. **29** (4), 398 (1993).
- ²⁹R.E. Setchell, J. Appl. Phys. **50**, 8186 (1979).
- ³⁰D.J. Steinberg, J. Phys. IV, **C3**, 837 (1991).
- ³¹D.J. Steinberg, Report No. UCRL-MA- 106439, Lawrence Livermore National Laboratory, Livermore, CA (1991).
- ³²Z. Rosenberg and Y. Partom, J. Appl. Phys. **58** (8), 3072 (1985).
- ³³B.L. Glushak and S.A. Novikov, Fizika Goreniya i Vzryva, **28** (1), 84 (1991) [Reproduced in Combust. Expl. Shock Waves **28** (1), 79 (1992)].
- ³⁴Y.V. Bat'kov, B.L. Glushak and S.A. Novikov, Fizika Goreniya i Vzryva, **25** (5), 126 (1988) [Reproduced in Combust. Expl. Shock Waves **25** (5), 635 (1989)].
- ³⁵J. Peng, F. Jing, D. Li and L. Wang, J. Appl. Phys. **98**, 013508 (2005).
- ³⁶D.J. Steinberg, S.G. Cochran and M.W. Guinan, J. Appl. Phys. **51** (3), 1498, (1980).
- ³⁷W.D. Reinhart, J.R. Asay, C.S. Alexander, L.C. Chabildas and B.J. Jensen, J. Dynamic Behavior Mater. **1**, 275 (2015).
- ³⁸J. Schroeder, J. non Cryst. Solids **40**, 549 (1980).
- ³⁹G.B. Hocker, Appl. Opt. **18** (9), 1445 (1979).
- ⁴⁰K. Vedam and R. Srinivasan, Acta Crysta. **22**, 630 (1967).
- ⁴¹W.W. Morey, G. Meltz and J.M. Weiss, 8th Optical Fiber Sensor (OFS) Conference, Monterey (CA), Postdeadline Paper PD-4.4 (1992).
- ⁴²F. Julich, L. Aulbach, A. Wilfert, P. Kratzer, R. Kuttler and J. Roths, Meas. Sci. Tech. **24**, 94007 (2013).
- ⁴³N.K. Sinha, Phys. Chem. Glass. **19** (4), 69 (1978).
- ⁴⁴A.J. Barlow and D.N. Payne, IEEE J. Quant. Electron. **19** (5), 834 (1983).
- ⁴⁵K. Matusita, C. Ihara, T. Komatsu and R. Yokota, J. Am. Ceram. Soc. **67** (10), 700 (1984).
- ⁴⁶Y. Namihara, J. Lightwave Technol. **3** (5), 1078 (1985).
- ⁴⁷A. Bertholds and R. Dändliker, J. Lightwave Technol. **6** (1), 17 (1988).
- ⁴⁸P.D. Dragic, J. Ballato, S. Morris and T. Hawkins, J. Opt. Soc. Am., **30** (2), 244 (2013).
- ⁴⁹M.S. Pambianchi, M. Dejneka, T. Gross, A. Ellison, S. Gomez, J. Price, Y. Feng, P. Tandom, D. Bookbinder and M.J. Li, "Corning Inc : Designing a new future with glass and optics", Ch. 1 in Material Research for Manufacturing, L.D. Madsen and E.B. Svedberg Ed., Springer Series in Materials Science **224** (2016).
- ⁵⁰N.F. Borelli and R.A Miller, Appl. Opt. **7** (5), 745 (1968).
- ⁵¹D.P. Dandekar, J. Appl. Phys. **84** (12), 6614 (1998).
- ⁵²J. Arndt and D. Stöffler, Phys. Chem. Glass., **10** (3), 117 (1969).
- ⁵³C.S. Zha, R.J. Hemley, H.K. Mao, T.S. Duffy and C. Meade, Phys. Rev., **50** (11), 13105 (1994).
- ⁵⁴H.M. Cohen and R. Roy, J. Am. Ceram. Soc., **44** (10), 523 (1961).
- ⁵⁵R. Roy and H.M. Cohen, Nature **190**, 798 (1961).
- ⁵⁶L.M. Barker and R.E. Hollenbach, J. Appl. Phys. **41**, 4208 (1970).
- ⁵⁷K. Kondo, S. Iio and A. Sawaoka, J. Appl. Phys. **52** (4), 2826 (1981).
- ⁵⁸K. Vedam, E.D.D. Schmidt and R. Roy, J. Am. Ceram. Soc. **49** (10), 531 (1966).
- ⁵⁹C. Meade and R. Jeanloz, Phys. Rev. B, **35** (1), 236 (1987).
- ⁶⁰X.F. Liu, R.J. Wang and W.H. Wang, Scripta. Mat. **62**, 254 (2010).
- ⁶¹T. Rouxel, H. Ji, T. Hammoud, and A. Moréac, Phys. Rev. Lett. **100**, 225501 (2008).
- ⁶²W.M. Isbell and D.R. Christman, DASA Report 2419, MSL-69-60 (1970).
- ⁶³H. Kogelnik, Bell Sys. Tech. J. **55** (1), 109 (1976).